STRUCTURES AND MAGNETIC PROPERTIES OF LOW-DIMENSIONAL SALTS

By

LIANG-KUEI CHOU

A DISSERTATION PRESENTED TO THE GRADUATE SCHOOL
OF THE UNIVERSITY OF FLORIDA IN PARTIAL FULFILLMENT
OF THE REQUIREMENTS FOR THE DEGREE OF
DOCTOR OF PHILOSOPHY

UNIVERSITY OF FLORIDA

1996

ACKNOWLEDGMENTS

When I arrived in Gainesville in August 1991, the first English I learned was, "Go, Gators!". I have lived in Gainesville longer than anywhere else, except my home town, Taipei. I must thank the chemistry department for giving me the chance to come here not only study chemistry, but to understand America's philosophy on life. I hope that I too have made a small contribution to the quality reputation of the Department of Chemistry at the University of Florida.

I have great appreciation for the guidance and support of my research director, Dr. Daniel R. Talham. From Dan, I have not only begun to learn the fun of chemistry, but the attitude of discovering and searching for new things in science.

I thank the members of my committee, Professors Russell S. Drago, James M. Boncella, William R. Dolbier, and Mark W. Meisel, for their time, advice and ecouragement. The research of this dissertation is greatly dependent on the assistance and many helpful conversations with Drs. Khalil Abboud, Manuel A. Quijada and W. W. Kim.

One can learn much from the people around one, and my fellow group members over the years have made that all too evident. Those who have made research so enjoyable are Glênnison de Oliveira, Marvin Clevenger, Brian Ward, Scott Whipps, Candace Seip, Gail Fanucci and Melissa Petruska. I also thank my friend, Hsiang-Lin Liu and Garret E. Granroth, who helped me a lot in understanding solid-state theory.

My parents, Chao-Feng and Chun-Chih, support me all the time. It really helps me a lot, whenever I get a call from them in Taiwan. Whenever I face difficulties, they always say "Hey, Chou, you have already washed your head half way, go ahead to finish it."

Finally I thank my wife, Yu-chi. Since I met her in 1986, she has always accompanied me in everything I do, even an NMR experiment. Whenever I have a difficult time with an experiment, she always encourages me and tells me " Don't give up."

TABLE OF CONTENTS

ACKNOWLEDGMENTS ii

ABSTRACT vi

CHAPTERS

1 BACKGROUND AND INTRODUCTION 1

One-Dimensional Heisenberg Antiferromagnets 1
Organic Cation-Radical Salts 10

2 SYNTHESIS, STRUCTURE AND MAGNETIC SUSCEPTIBILITY OF TETRAMETHYLAMMONOIUM NICKEL NITRITE, $(CH_3)_4N[Ni(NO_2)_3]$: AN S = 1 ONE-DIMENSIONAL HEISENBERG ANTIFERROMAGNET 19

Experimental Section 20
Synthesis of Tetramethylammonium Nickel Nitrite (TMNIN) 20
Crystallographic Data Collection and Structure Determination 20
Magnetic Measurements 21
Results and Discussion 22
TMNIN Structure 22
Magnetic Susceptibility 27
Conclusions 30

3 THE SYNTHESIS, STRUCTURE, MAGNETIC SUSCEPTIBILITY AND SOME PHYSICAL CHARACTERISTICS OF $Ni(C_3H_{10}N_2)_2N_3(ClO_4)$, NINAZ 31

Experimental Section 33
The Synthesis of *bis*(propylenediamine)azidonickel (II) perchlorate 33
Ultra-fine Powder NINAZ 43
Magnetic Measurements 43
ESR Measurements 46
Elemental Analysis 46
Results and Discussion 47
NINAZ Structure 47
Haldane Gap in NINAZ-d_{20} 52
Magnetic Susceptibility 52
ESR Result 55
Conclusions 68

4 DICATION SALTS OF THE ORGANIC DONOR BIS(ETHYLENEDITHIO)TETRATHIAFULVALENE 71

Experimental Section 72
Materials 72
BEDT-TTF(BF_4)$_2$ 73
BEDT-TTF(ClO_4)$_2$ 76
Crystallographic Data Collection and Structure Determination 76
Optical Measurement 77
Results and Discussion 78
Synthesis and Structure 78
Optical Properties 85
Conclusions 85

5 STRUCTURE, MAGNETIC, OPTICAL, AND TRANSPORT PROPERTIES OF (BEDT-TTF)PF_6* 91

Introduction 91
Experimental Section 93
Materials 93
(BEDT-TTF)PF_6*, δ-(BEDT-TTF)PF_6, and ε-(BEDT-TTF)PF_6 93
Crystallographic Data Collection and Structure Determination 93
Temperature-dependent ESR Experiment 95
Transport Measurement 96
Optical Measurement 97
Magnetic Measurement 98
Results 98
Synthesis and Structure 98
Optical Measurement 99
Conductivity 110
ESR Measurement 115
Magnetic Susceptibility Measurement 120
Discussion 120
Structure 120
Magnetic Data 123
Conclusions 123

APPENDIX 124

TABLES OF CRYSTALLOGRAPHIC DATA 125

LIST OF REFERENCES 154

BIOGRAPHICAL SKETCH 160

Abstract of Dissertation Presented to the Graduate School
of the University of Florida in Partial Fulfillment of the
Requirements for the Degree of Doctor of Philosophy

STRUCTURES AND MAGNETIC PROPERTIES OF LOW-DIMENSIONAL SALTS

By

Liang-Kuei Chou

May, 1996

Chairman: Daniel R. Talham
Major Department: Chemistry

This dissertation presents experimental results from the synthesis, structure determination, magnetic, and electronic properties characterizations of two types of low-dimensional salts. The first class of materials are one-dimensional nickel (II) chain compounds, and the second type of materials are BEDT-TTF cation-radical salts. The crystal structure of tetramethylammonium nickelnitrite, $(CH_3)_4N[Ni(NO_2)_3]$ (TMNIN) was determined by X-ray diffraction at room temperature. The structure of TMNIN consists of infinite chains of Ni^{2+} ions with adjacent Ni^{2+} ions bridged by three cis-μ-nitro ligands. Alternate Ni^{2+} ions along the chain are chemically distinct with Ni1 octahedrally coordinated with six nitrite nitrogens, and the adjacent Ni2 is octahedrally coordinated with six nitrite oxygens. The tetramethylammonium ions are located in positions along the 3-fold rotation axes and form channels that separate the Ni chains. From the magnetic susceptibility data, TMNIN is identified as a one-dimensional Heisenberg antiferromagnet. The data are interpreted in the context of Haldane Gap materials.

Bis(propylenediamine)azidonickel (II) perchlorate, $Ni(C_3H_{10}N_2)_2N_3(ClO_4)$

(NINAZ) is another quasi-one-dimensional chain compound. The synthetic method to NINAZ has been improved and large pure single crystals (1.5 cm X 1.5 cm X 0.2 cm) have been obtained. Deuterated NINAZ has also been synthesized in order to measure the Haldane Gap with neutron inelastic scattering. The magnetic properties as a function of particle size have been investigated.

Dication salts of the organic donor *bis*(ethylenedithio)tetrathiafulvalene (BEDT-TTF) have been isolated as BF_4^- and ClO_4^- salts. They are the first examples of salts where BEDT-TTF appears only as dication. Bond length data from X-ray structure determinations of the dication salts were used as standards for assigning the +2 oxidation state to BEDT-TTF molecules in mixed valence cation-radical salts. Optical spectroscopy shows that during the electrocrystallization BEDT-TTF is slowly oxidized by $ClCH_2COCl$, indicating $(BEDT\text{-}TTF)^+$ is first formed in the electrolytic medium before electrochemical oxidation to the dication and precipitation with the electrolyte anion.

The new compound $(BEDT\text{-}TTF)PF_6^*$ has also been prepared by electrocrystallization methods, and the crystal structure was determined by X-ray diffraction at room temperature and 173K. Unlike a similar salt, δ-$(BEDT\text{-}TTF)PF_6$, there is no dimerization of the donor molecules at room temperature in $(BEDT\text{-}TTF)PF_6^*$. A structural phase transition at 260K has been assigned to anion ordering. From the conductivity, ESR and optical data, we conclude that $(BEDT\text{-}TTF)PF_6^*$ is a Mott-Hubbard insulator. A low temperature magnetic transition is discussed in terms of a spin-Peierls transition.

CHAPTER 1
BACKGROUND AND INTRODUCTION

This dissertation presents the experimental results from the synthesis, structure determination, magnetic, and electronic properties characterizations of two types of low-dimensional salts. The first are one-dimensional nickel (II) chain materials, and the second type of material is BEDT-TTF cation-radical salts. Chapter 1 will provide a literature review on the quasi-one-dimensional S=1/2 and S=1 chain compounds and cation-radical molecular solids based on bis(ethylenedithio)tetrathiafulvalene (BEDT-TTF). Chapter 2 will describe the synthesis, structure and magnetic susceptibility of tetramethylammonium nickel nitrite (TMNIN), $(CH_3)_4N[Ni(NO_2)_3]$, an S=1 one-dimensional Heisenberg antiferromagnet. Chapter 3 will describe the synthesis, structure, and magnetic properties of *bis*(propylenediamine)azidonickel (II) perchlorate (NINAZ) $Ni(C_3H_{10}N_2)_2N_3(ClO_4)$. Chapter 4 will present the synthesis, structures, and optical properties of dication salts of BEDT-TTF. Chapter 5 will present the synthesis, structures, conductivities, and temperature-dependent ESR measurements of (BEDT-TTF)PF_6* and δ-(BEDT-TTF)PF_6.

One-Dimensional Heisenberg Antiferromagnets

The chemical realization of quasi-one-dimensional (quasi-1D) materials has allowed for detailed experimental investigations probing the physical theories that describe electronic and magnetic properties in low-dimensional solids.[1] An understanding of physical phenomena in quasi--1D solids has led to the development of a number of conducting,[2] superconducting,[3] and magnetic materials[4] based on low-dimensional

structures. In 1983, Haldane suggested[5] that a one-dimensional Heisenberg antiferromagnet (1D HAF) with integer spin possessed an energy gap between the nonmagnetic ground state and the first excited state. In noninteger spin systems, there is no energy gap between the ground state and first excited state. The magnetic susceptibility behavior of S=1/2 and S=1 one-dimensional Heisenberg systems are very different. The susceptibility results for a spin S=1/2 Heisenberg linear chain have been described by Bonner and Fisher.[6] A broad maximum in the susceptibility is predicted, as illustrated in Figure 1.1. For S=1/2, the susceptibility maximum will have value

$$\frac{\chi_{max}}{Ng^2\mu^2 / |J|} = 0.07346$$

at the temperature

$$kT_{max} / |J| = 1.282$$

According to Bonner and Fisher theory, when the temperature approaches 0 K, the susceptibility of (S=1/2) noninteger systems will have finite value. This theory has been applied to a very large number of samples;[7] for example, fits of the susceptibilities of $[Cu(NH_3)_4](NO_3)_2$ [8] are shown in Figure 1.2. Another example of an antiferromagnetic Heisenberg chain compound (S= noninteger) is $[N(CH_3)_4]MnCl_3$, TMMC, the structure[9] of which is illustrated in Fig. 1.3. The crystal consists of chains of S= 5/2 manganese atoms bridged by three chloride ions; the closest distance between manganese ions in different chains is 0.915 nm. The intrachain exchange constant J / k is about -6.7 K. In the integer spin (S= 1,2) Heisenberg systems, as the temperature approaches absolute zero K, the susceptibilities approach to zero. To date, the few systems that are believed to be Haldane materials include the Ni^{2+} linear chain compounds $[Ni(C_2H_8N_2)_2NO_2]ClO_4$

Figure 1-1. The (reduced) Bonner-Fisher susceptibility.[6]

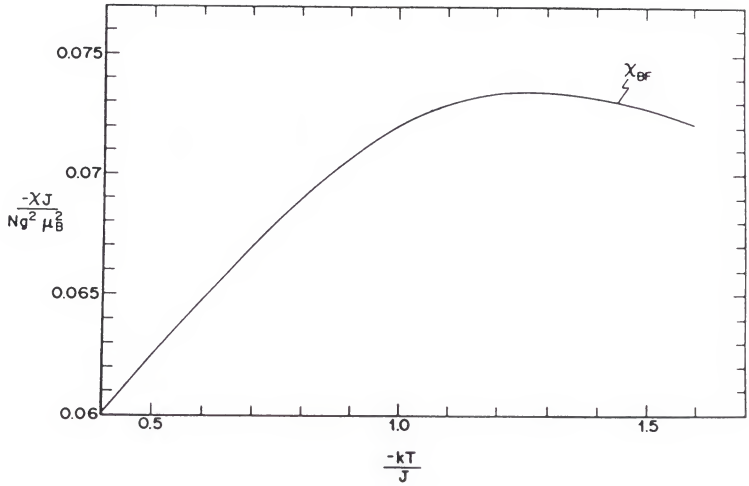
0.075
0.07
0.065
0.06
$\frac{-\chi J}{Ng^2\mu_B^2}$
χ_{BF}
0.5
1.0
1.5
$\frac{-kT}{J}$

Figure 1-2. The three orthogonal susceptibilities of $[Cu(NH_3)_4](NO_3)_2$ (CTN), along with the best fit to the data.[8]

χ (emu / mole)
0.03
.02
.01
0
5
10
15
20
o = χa
• = χb
x = χc
Cu (NH3)4 (NO3)2

Figure 1-3. A sketch of the linear chains found in $(CH_3)_4NMnCl_3$. The octahedral enviroment about the manganse atom is slightly distorted, corresponding to a lengthening along the chain.[9]

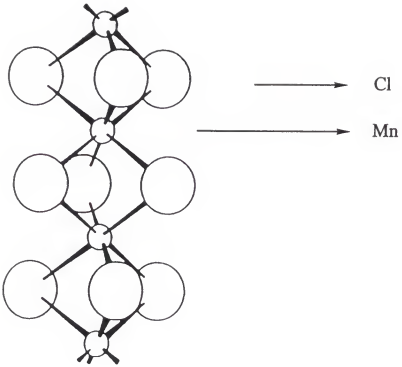
Cl
Mn

(NENP),[10] $[Ni(C_3H_{10}N_2)_2NO_2]ClO_4$ (NINO),[11] $[Ni(C_3H_{10}N_2)_2N_3]ClO_4$ (NINAZ),[12] $(CH_3)_4N[Ni(NO_2)_3]$ (TMNIN),[13] and $RbNiCl_3$ [14] and $AgVP_2S_6$.[11] Nightingale and Blote[15] have provided a reliable estimation of the Haldane gap as $Eg = 0.41 \times |J_{intra}|$, where J_{intra} is the coupling constant between the nearest neighbors in the chain with the 1-dimensional Heisenberg hamiltonian: $-2J \Sigma S_i S_{i+1}$. Affleck[16] have performed numerical calculations for the Heisenberg model and their results support the Haldane prediction.

According to Haldane's prediction, Haldane gap materials should have the following characteristics.

1. The system should have a good one-dimensional enviroment, and the ratio of $|J_{intra} / J_{inter}|$ should be large, where J_{inter} is the coupling constant between spin sites of neighboring chains. The chains should be well separated from one another so that there is no three-dimensional long range magnetic order in this system.

2. The intrachain exchange should be nearly isotropic, and the ratio of $|D/J_{intra}|$ must be very small.[17] Here, D is the single ion anisotropy.

3. The value of J_{intra} should be constant along the chain, which implies the crystallographic structure should be uniform along the whole chain. Alternating Heisenberg linear chain materials are not Haldane gap materials.

In Haldane gap materials, the following experimental results will be observed:

1. The temperature-dependent magnetic susceptibilty will approach zero, as the temperature approaches absolute zero.

2. The Haldane gap is directly measurable by inelastic neutron scattering.[18]

3. The slope of the magnetization curve, $M = f(H)$, will present a discontinuity when the field reaches a critical value, $Hc = E_G / g\mu_B$, when the lowest component ($M_s = -1$) of the first excited triplet state crosses the singlet ground state.[19]

In order to study Haldane gap materials, synthesis of appropriate high quality crystals is the first step. In chapter 2 and chapter 3, we will discuss the experimental results for TMNIN and NINAZ.

Organic Cation-Radical Salts

Organic cation-radical salts have been a subject of interest for years. Bis(ethylenedithio)tetrathiafulvalene (BEDT-TTF or ET) (Figure 1-4) is the most extensively used electron-donor molecule in the search for new organic superconductors. More than ten BEDT-TTF-based ambient-pressure superconductors have been found to date, including that with the highest superconducting transition temperature (T_c) of any cation-radical salt i.e., κ-$(ET)_2Cu[N(CN)_2]Br$, with a T_c equal to 12.5 K.[20]

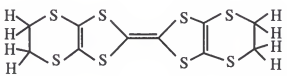

Figure 1-4. BEDT-TTF

The cation-radical salts of BEDT-TTF are complex due to the formation of multiple structural phases, often with varied stoichiometries. For example, there are four (α, θ, β, κ)[21] (Figure 1-5) structurally unique phases known for BEDT-TTF-triiodide salts with 2:1 stoichiometry.

While the α-phase[22] is a metal with a metal-insulator transition at 135 K, the three remaining phases are ambient pressure superconductors with T_c = 3.6 K,[23] 1.5 K[24] (8 K, 0.5 kbar) and 3.6 K,[25] for the θ, β, and κ phases, respectively.

Figure 1-5. Packing schemes of BEDT-TTF molecules, viewed along molecular axis, in α, β, θ, and κ phases of $(ET)_2I_3$. [21]

alpha

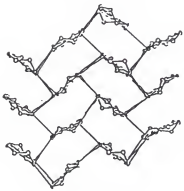

beta

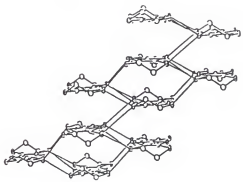

theta

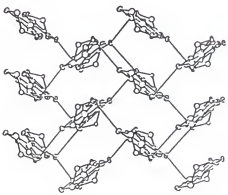

kappa

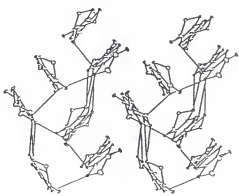

The structure property correlations in the series β-(BEDT-TTF)$_2$X,[26] (X = I_3^-, AuI_2^-, I_2Br^-, IBr_2^-) has been established by Williams et al.[27] According to their results, the larger anions form higher T_c superconductors in the β-form BEDT-TTF salts, because the larger anions form good interactions between the ethylene groups of BEDT-TTF and the anions. While investigating larger anions, Williams et al.[28] obtained the polymeric anion BEDT-TTF conductors, (BEDT-TTF)$Ag_4(CN)_5$ [29] and (BEDT-TTF)$Ag_{6.4}I_8$.[30] From here, larger anions[20] $Cu(NCS)_2^-$ and $Cu[N(CN)_2]Br^-$ were synthesized.

The Tc of κ-(BEDT-TTF)$_2$Cu(NCS)$_2$ and κ-(BEDT-TTF)$_2$Cu[N(CN)$_2$]Br are 10.4 K and 12.5 K, respectively. The polymeric anion BEDT-TTF salts belong to an entirely different structural class than the β-phase BEDT-TTF salts. The structure of κ-type packing in BEDT-TTF salts contains orthogonally arranged molecular dimers rather than a corrugated-sheet network (Figure 1-6).[31] The anions in the κ-(BEDT-TTF)$_2$Cu[N(CN)$_2$]Br salt consist of a polymeric mixed (halide)(pseudohalide)cuprate (I) species. The anions contain infinite zig-zag chains of ---Cu-dicyanamide-Cu---units, and the copper atoms complete their coordination spheres with the bromine atom (Figure 1-7).[32] Trigonal coordination around Cu^+ is also observed in κ-(BEDT-TTF)$_2$Cu(NCS)$_2$ (Figure 1-8).[33]

In the study of high T_c superconductors, Pickett et al.[34] have changed the percent doping in order to change the conductivities and magnetic properties. The dopant concentration determines the degree of band filling, and Figure 1-9 then demonstrate that the properties of the high T_c systems have been thoroughly investigated as a function of their degree of band filling. A similar phase diagram does not exist for any of the classes of organic superconductors. In fact, the effect of band filling in the organic conductors has scarcely been probed. In the typical 2:1 salts of the BEDT-TTF or TMTXF (X = S, Se) series with monovalent anions, the charge on the donor molecule of +1/2 results in a 3/4 filled band. Of all of the known organic superconductors, only (BEDT-TTF)$_3Cl_2.H_2O$ has a stoichiometry differing from 2:1. [21] While there are many other examples of BEDT-TTF

Figure 1-6. The packing of BEDT-TTF in κ-(BEDT-TTF)$_2$Cu[N(CN)$_2$]Br. [31]

Figure 1-7. The anions in κ-(BEDT-TTF)$_2$Cu[N(CN)$_2$]Br. [32]

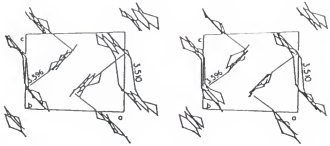
3.96
3.55
3.96
3.55

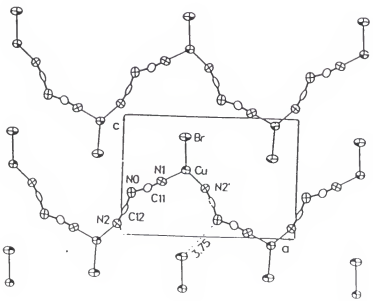
c
Br
N1
Cu
N0
C11
N2'
N2
C12
3.75
a

Figure 1-8. Crystal structure of κ-(BEDT-TTF)$_2$[Cu(NCS)$_2$]. [33]

Figure 1-9. Composition phase diagram for the LaSrCuO "high-T_c system. [34]

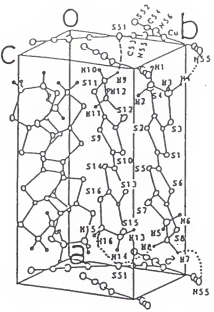
O
b
C

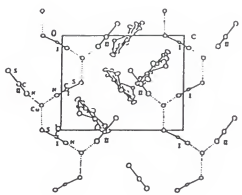

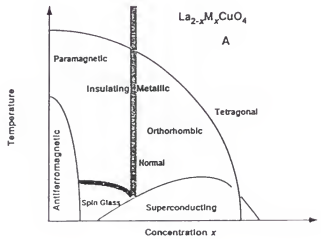
La2-xMxCuO4
A
Paramagnetic
Insulating
Metallic
Tetragonal
Orthorhombic
Normal
Antiferromagnetic
Spin Glass
Superconducting
Temperature
Concentration x

structural motifs, and several different band-structures observed for BEDT-TTF salts, they all have in common a charge on the donor molecule of less than or equal to +1.

Chapter 4, describes isolation of salts of the $(BEDT\text{-}TTF)^{2+}$ ion with BF_4^- and ClO_4^- counterions showing that high-oxidation states of BEDT-TTF are stable. This is the first time that a definative structure of $(BEDT\text{-}TTF)^{2+}$ has been determined, and will now allow greater certainty in using structural data to assess the degree of oxidation in charge transfer salts of the BEDT-TTF donor.

Possible method to modify the packing of BEDT-TTF molecules in the solid-state is to insert small molecules into the BEDT-TTF cation-radical salts. For example, in the structure $(BEDT\text{-}TTF)_2PF_6{\cdot}ClCH_2COCl$, the BEDT-TTF packing is different than observed in other PF_6^- salts and is similar to that seen in the conductor β'-$(BEDT\text{-}TTF)_2AuBr_2$.[35] Using this idea we tried adding CS_2 to the solvent system used to isolate β-$(BEDT\text{-}TTF)PF_6$. The result of adding CS_2 to the system was not the incorporation of CS_2 into the structure, but the isolation of a new salt, $(BEDT\text{-}TTF)PF_6$*. In chapter 5, we will describe the synthesis, temperature-dependent ESR, conductivity and structure of $(BEDT\text{-}TTF)PF_6$*.

CHAPTER 2
SYNTHESIS, STRUCTURE AND MAGNETIC SUSCEPTIBILITY OF TETRAMETHYLAMMONIUM NICKEL NITRITE, $(CH_3)_4N[Ni(NO_2)_3]$: AN S = 1 ONE-DIMENSIONAL HEISENBERG ANTIFERROMAGNET

Since the predictions of Haldane,[5] one-dimensional Heisenberg antiferromagnets (1D-HAF) with integer spin have been the subjects of numerous experimental investigations.[11] Recently, tetramethylammonium nickel nitrite, $(CH_3)_4N[Ni(NO_2)_3]$ (TMNIN),[13] was shown to possess properties which are consistent with a Haldane gap; however, the structure of TMNIN has never been clarified. On the basis of IR, X-ray absorption, and X-ray diffraction studies, Gadet et al.[38] were able to determine that the TMNIN structure consists of infinite chains of Ni^{2+} ions separated from one another by channels of tetramethylammonium cations. Adjacent metal ions within a chain are bridged by three nitrite ligands where the mode of bridging is Ni-N(O)O-Ni and is cis with respect to the N-O bond (cis-μ-nitro).[39] However, due to structural disorder or possible crystal twinning, the structure was not resolved with certainty. In this chapter, the preparation and crystal structure of TMNIN are described. The crystal structure determination shows that the one-dimensional chains are comprised of alternating NiO_6 and NiN_6 octahedra. Magnetic susceptibility data as a function of sample orientation is also presented for TMNIN from 1.8 to 300 K.

The following experimental results have already been published in ref. 13, 36, and 37.

Experimental Section

Synthesis of Tetramethylammonium Nickel Nitrite (TMNIN)

Tetramethylammonium nickel nitrite, $(CH_3)_4N[Ni(NO_2)_3]$, was prepared according to the procedure described by Goodgame and Hitchman.[40] Two different procedures were used to grow crystals. Method 1 yielded crystals suitable for structure determination by slowly adding a solution of 0.11g(5×10^{-4} mol) of $NiBr_2$ and 0.077g(5×10^{-4} mol) of $(CH_3)_4NBr$ in 0.6 mL of H_2O on top of a solution of 0.33 g (5×10^{-3} mol) of $NaNO_2$ in 1.0 mL of H_2O. After 4-6 days at room temperature, the yellow-brown crystals formed on the sides of the test tube. Crystals were rinsed with cold water and dried overnight in a desiccator. Anal. Calad for $C_4H_{12}N_4NiO_6$: C, 17.73; H, 4.43; N, 20.68. Found: C, 17.65; H, 4.49; N, 20.54. Larger crystals (typically 0.4 mm x 0.15 mm x 0.15 mm) were obtained by slowly adding a solution of 0.11g(1.67×10^{-4} mol) of $NiBr_2$ and 0.077g(1.67×10^{-4} mol) of $(CH_3)_4NBr$ in 1.8 mL of H_2O on top of a solution of 0.33g (1.67×10^{-3} mol) of $NaNO_2$ in 3.0mL of H_2O. After 4 months at refrigerator temperature (11°C), the yellow-brown crystals formed on the bottoms of the test tube. Crystals were rinsed with cold water and dried overnight in a desiccator. Found: C, 17.62; H, 4.46; N, 20.60.

Crystallographic Data Collection and Structure Determination

The X-ray measurement was completed by Dr. Khalil A. Abboud. For the structure reported here, a very small yellow crystal of dimensions 0.30 mm x 0.04 mm x 0.04 mm was chosen to avoid selecting a multiple crystal. Data were collected at room temperature on a Siemens R3m/V diffractometer equipped with a graphite monochromator utilizing Mo Kα radiation ($\lambda = 0.71073$ Å). A total of 32 reflections with $20.0^\circ < 2\theta < 22.0^\circ$ were used to refine the cell parameters, and 2497 reflections were collected using the

ω-scan method. Four reflections (231,302,231,302) were measured every 96 reflections to monitor instrument and crystal stability (maximun correction on I was < 1%). Absorption corrections were applied based on measured crystal faces using SHELXTL plus;[41] absorption coefficient, $\mu = 1.93$ mm^{-1} (minimum and maximum transmission factors are 0.613 and 0.931, respectively). Examination of equivalent reflections showed that the crystal system is trigonal and that the Laue group is P3m. A set of data ($h \pm k \pm l$) was collected, and the structure was solved in the space group P3m1 using the heavy atom method in SHELXTL plus[41] from which the location of the Ni atoms (in special positions along the c axis; 000 and 001/2) were obtained. The rest of the non-H atoms were obtained from a subsequent Difference Fourier map. The structure was refined in SHELXTL plus using full-matrix least-squares. The non-H atoms were treated anisotropically and the H atoms were refined with isotropic thermal parameters. In the final cycle of refinement, 359 reflections with $I > 2\sigma(I)$ and 45 parameters yielded values for R and ωR of 0.0250 and 0.0282, respectively. The linear absorption coefficient was calculated from values from the *International Tables for X-ray Crystallography*.[42] Scattering factors for non-hydrogen atoms were taken from Cromer and Mann[43] with anomalous-dispersion corrections from Cromer and Liberman,[44] while those for hydrogen atoms were from Stewart et al.[45] Crystal data are presented in Appendix Table A-1. Fractional coordinates and isotropic thermal parameters for the non-H atoms are given in Appendix Table A-2, and bond lengths and angles are given in Appendix Table A-3.

Magnetic Measurements

Measurements on TMNIN were performed in collaboration with our physics colleaques and have been reported by Granroth et al. [36, 37] The temperature dependence of the magnetic susceptibility was obtained from magnetization measurements made with a Quantum Design (San Diego, CA) Model MPMS magnetometer operating at 0.5 Tesla. A

2.1mg bundle of crystals was held together by a small quantity of "fingernail polish", and pieces of plastic straw were used as sample holder during the measurements. The magnetic signal arising from the plastic is well characterized and has been subtracted from the results.

Results and Discussion

TMNIN Structure

The structure consists of infinite chains of Ni atoms along the c axis, Figure 2-1, linked by bridging NO_2 ligands such that alternate Ni ions along a chain are chemically distinct with Ni1 octahedrally coordinated with six nitrite nitrogens, and the adjacent Ni2 octahedrally coordinated with six nitrite oxygens. The Ni ions are evenly spaced along the chain and are separated by one-half the cell edge or 3.541 Å. The tetramethylammonium ions are located in positions along the 3-fold rotation axes where the N atoms occupy positions 1/3, 2/3, z and 2/3, 1/3, z', with one C atom on the 3-fold rotation axis and another on the mirror plane passing through the 3-fold axis. The counterions separate the Ni chains, and the closest interchain Ni-Ni distance is equal to the cell edge of 9.1029 Å. A packing diagram, showing the location of the tetramethylammonium counterions and the interchain separations, is given in Figure 2-2. The nitrite geometry is consistent with that found in other cis-μ-nitro nickel complexes,[46] with the bond from nitrogen to the bonding oxygen longer than the bond to the nonbonding oxygen. The ONO bond angle is 115°. The nonligating nitrite O atoms are closer to the nitrogen-coordinated Ni1 than to the oxygen-coordinated Ni2 and form a space for the tetramethylammonium ions. Since the two Ni ions are chemically inequivalent, the tetramethylammonium ions lie closer to the oxygen-coordinated nickel (N-Ni2 distance is 5.363 Å) than to the nitrogen-coordinated

Figure 2-1. View perpendicular to the c axis of a portion of the Ni chain in TMNIN. Alternating Ni sites are octahedrally coordinated by N atoms (Ni1) and O atoms (Ni2) of the bridging nitrite ligands. Nickel chains are separated by columns of tetramethylammonium counterions. Two tetramethylammonium ions from different colums are shown; others are omitted for clarity. Atoms are represented by 50% probability ellipsoids.[13]

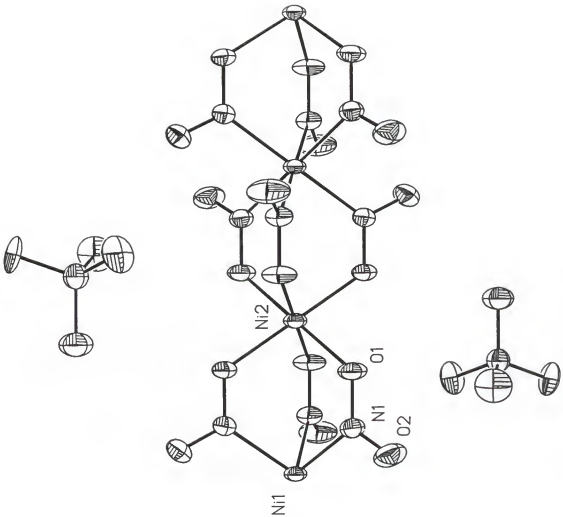
Ni2
O1
N1
O2
Ni1

Figure 2-2. Packing diagram for TMNIN viewed along the c axis showing the separated nickel chains. Intrachain Ni-Ni distances are 3.541 Å, while the interchain distance is 9.1029 Å.[13]

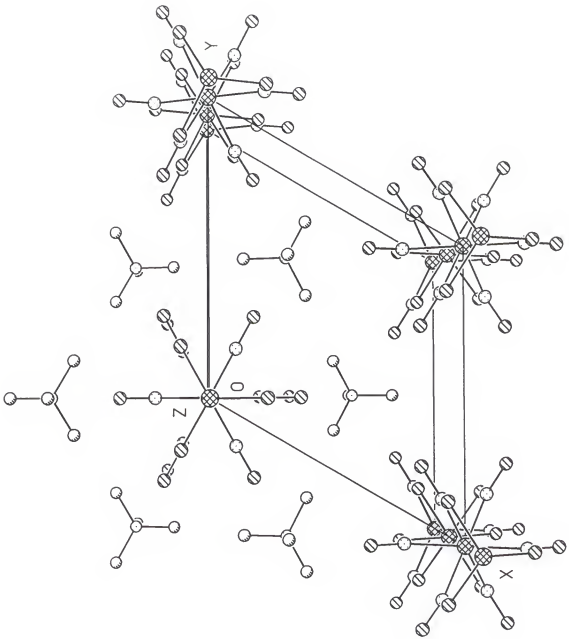
Y
Z
O
X

nickel (N-Ni1 distance is 5.809 Å). The NiN_6 and NiO_6 octahedra are distorted, as shared faces along the chain slightly flatten each octahedron. The distortion is less in the NiN6 octahedron to minimize crowding of nonbonding nitrite oxygens. This is in contrast to the axial distortions seen in the hexagonal $MNiX_3$ (M= Cs, Rb, $N(CH_3)_4$; X = Cl, Br) compounds that are also comprised of 1D chains formed from face-sharing octahedra.[47] In the $MNiX_3$ series, the MX_6 octahedra are elongated along the chain axis in order to minimize the Ni-Ni Coulomb repulsions.[48] In TMNIN, each NO_2 plane bisects the angle between the perpendicular axes of the NiN_6 and NiO_6 octahedron that it coordinates. Normally, in nitrite binding, the NO_2 plane is parallel to one of the perpendicular axes in order to maximize π-overlap with the metal. The poor metal-ligand π-overlap in TMNIN is consistent with its low value of magnetic exchange[38] ($J/k_B \approx -10$ K, see Magnetic Susceptibility part) despite the short Ni-Ni distance. For comparison, in NENP where the bridging NO_2 ligand is aligned for good π-overlap, $J/k_B = -48$ K, despite the longer Ni-Ni separation of 5.15 Å.[49]

Magnetic Susceptibility

Susceptibility vs temperature data from 1.8 to 300 K for a 2.1 mg bundle of single crystals, aligned with their chain axes parallel, are presented in Figure 2-3 for two orientations of the bundle with respect to the magnetic field. The susceptibility rises as the temperature decreases, reaching a maximum around 14 K, and then sharply decreases down to 1.8 K. The shape of the susceptibility plot is similar to that seen for a multicrystalline sample[38] and is characteristic of a Haldane gap system with the susceptibility approaching zero as $T \rightarrow 0$.[38] The data reveal a slight anisotropy in the susceptibility for the two orientations shown in figure 2-3. Above T = 6 K, the data are fit with an analytical expression[50] (eq 2-1) derived from the numerical studies of Weng[51] for the susceptibility of an S = 1 Heisenberg chain:

Figure 2-3. Magnetic susceptibility, χ, is plotted as a function of temperature, T, for the cases where the magnetic field of 0.5 T is oriented parallel (top) and perpendicular (bottom) to the TMNIN chain axis.[13]

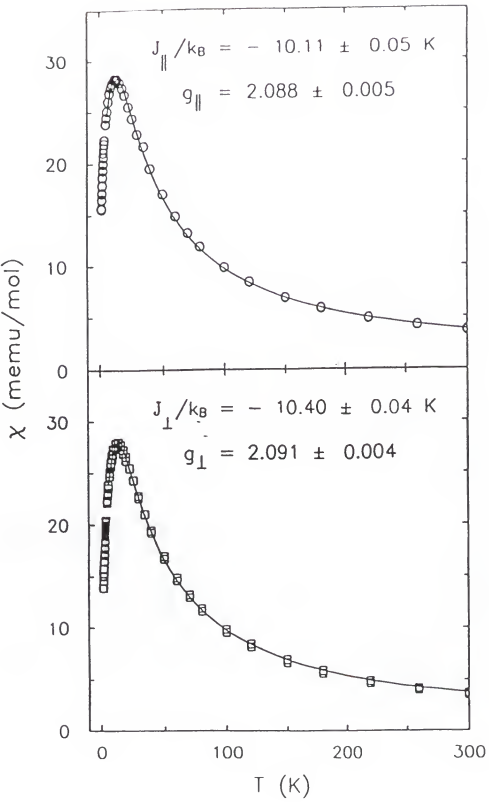
$J_{\parallel}/k_B$ = − 10.11 ± 0.05 K
$g_{\parallel}$ = 2.088 ± 0.005
$J_{\perp}/k_B$ = − 10.40 ± 0.04 K
$g_{\perp}$ = 2.091 ± 0.004
χ (memu/mol)
T (K)
0
10
20
30
100
200
300

$$\frac{X_M kT}{N(g\mu_B)^2} = \frac{2 + 0.0194x + 0.777x^2}{3 + 4.346x + 3.232x^2 + 5.834x^3} \qquad (2\text{-}1)$$

where $x = J/kT$.[51] Weng's results are based on the simple Hamiltonian, $H = -J\Sigma S_i S_{i+1}$, and ignore the signal ion anisotropy terms $D(S_i^Z)^2$ and $E\{(S_i^x)^2 - (S_i^y)^2\}$ that represent the axial and rhombic distortions from cubic symmetry, respectively. Nolinear least-squares fits of the data for $T > 6$ K yield, for $H_{//}$ c axis, $g_{//} = 2.088 \pm 0.005$, $J/k_B = -10.11 \pm 0.05$ K, and for $H_\perp$ c axis, $g_\perp = 2.091 \pm 0.004$, $J/k_B = -10.40 \pm 0.04$ K where the listed uncertainties are 1 σ statistical errors derived from the fitting procedure and do not represent systematic errors that may be present in the data, such as those related to the subtraction of the background contributions.

To date, there is no explicit expression for the temperature-dependent susceptibility of a linear chain S = 1 Heisenberg antiferromagnet over a broad temperature range that includes the single ion anisotropy terms. However, the axial distortion parameter, D, for a trigonal or tetragonal distortion can be estimated from the orientational difference in g values according to the expression[52,53]

$$D = \lambda/2(g_{//} - g_\perp) \qquad (2\text{-}2)$$

where λ is the spin-orbit coupling parameter. By using the g values determined from the fits to the susceptibility data in figure 2-3 and taking λ as -360 K,[52,53] a coarse estimate of $D/k_B = 0.5 \pm 1.2$ K is obtained. This value is only an estimate, but is consistent with recent EPR work which places an upper bound on $|D|$ to be less than 1 K.[54]

Conclusions

The crystal structure of TMNIN is unique when compared to other materials possessing a Haldane gap. The alternating pattern of two distinct Ni ions allows the magnetic interactions to be characterized by one nearest-neighbor (J), and two different next nearest-neighbor interactions.

CHAPTER 3
THE SYNTHESIS, STRUCTURE, MAGNETIC SUSCEPTIBILITY AND SOME PHYSICAL CHARACTERISTICS OF $Ni(C_3H_{10}N_2)_2N_3(ClO_4)$, NINAZ#

In the past few years, one-dimensional Heisenberg antiferromagnets (1D-HAF) with integer spin have been the subjects of numerous theroetical and experimental investigations.[11] The interest in 1D-HAF has been strongly renewed by the Haldane conjecture.[5] The first attempts at observing the Haldane gap were neutron scattering experiments in $CsNiCl_3$.[56] This compound has a relatively large interchain exchange which induces 3D-AF long range order at T = 4.85 K and thus forbids the clear observation of the gap at low temperature. Renard et al.[18] have performed magnetic and neutron-diffraction experiments on NENP and NINO with the chemical formulas $Ni(C_2H_8N_2)NO_2(ClO_4)$ and $Ni(C_3H_{10}N_2)NO_2(ClO_4)$, respectively, which are regarded as better materials for testing the gap.

Another Ni chain compound, $Ni(C_3H_{10}N_2)_2N_3(ClO_4)$ (NINAZ), is believed to possess a Haldane gap. In this chapter, we describe modifications of the published synthetic method that lead to pure and large single crystals (1.5 cm X 1.5 cm X 0.2 cm). These materials make it possible to measure the Haldane Gap by neutron inelastic scattering (INS). However, in INS, the hydrogen atoms in NINAZ will cause too strong of a backround in the dispersion curve of magnetic excitations of NINAZ. We have therefore synthesized deuterated NINAZ in order to measure the Haldane Gap with INS.

Part of the following experiment results have already been published in ref. 55.

One theoretical treatment of one-dimensional Heisenberg antiferromagnetic chains by Affleck[57] is called a valence bond solid (VBS) model. In this model the spin 1 on each site is represented by symmetrization of two spin S = 1/2 variables. For a closed chain, the many-body S = 0 ground state is then formed by two valence bonds originating from each site to form singlets with adjacent neighbors. For an open chain (see Fig 3- 1), however, unpaired bonds are left at each end of the chain which remarkably correspond to effective fractional spins S = 1/2 at the ends of the chain. The presence of S = 1/2 end-chain spins has been seen in susceptibility, $\chi(T)$,[49] and ESR[58] investigations of doped NENP.

Figure 3-1. The spin-1 valence-bond-solid state.

We also report on the temperature dependent magnetic susceptibility and ESR measurements of NINAZ. The magnetic susceptibility measurement has been studied from 300K to 60mK. Below 1.5K, a large increase in susceptibility has been observed in single crystal, powdered, and ultrafine samples. ESR measurements have been studied from 300K to 4K. Below 10 K, an ESR signal is observed in single crystal, powdered, and ultrafine powdered samples. The results indicate that a large increase in the susceptibility below 1.5 K has been observed in our sample, our results are interpreted in terms of prensence of end-chain effects.

Experimental Section

The Synthesis of *bis*(propylenediamine)azidonickel (II) perchlorate (NINAZ)

Materials Nickel(II) perchlorate hexahydrate ($Ni(ClO_4)_2.6H_2O$,), 1,3-diaminopropane ($H_2N(CH_2)_3NH_2$, 99%)(pn), and sodium azide (NaN_3, 99%) were purchased from Aldrich Chemical Co. (Milwaukee, WI).

Bis(propylenediamine)azidonickel (II) perchlorate (NINAZ) NINAZ was prepared using a modification of the procedure described by Gadet *et al* .[59] A solution of 1,3-diaminopropane (0.835 ml, 1.2 x 10^{-2} mole) in 5 ml H_2O was added dropwise to 1.83 g nickel (II) perchlorate hexahydrate dissolved in 30 ml H_2O to form the $Ni(C_3H_{10}N_2)_2(ClO_4)_2$ intermediate. The addition was done slowly over 10 minutes to avoid forming $Ni(C_3H_{10}N_2)_3(ClO_4)_2$. Sodium azide (0.325 g, 5 x 10^{-3} mole) dissolved in 4 ml H_2O was then added to the $Ni(C_3H_{10}N_2)_2(ClO_4)_2$ solution. At this point, a few extra drops of 1,3-diaminopropane were added and the solution was put aside to evaporate. The excess diaminopropane minimized formation of by-product bis(propylenediamine)diazidonickel (II) (NIBAZ). After 3 weeks, well-shaped hexagonal deep blue single crystals of NINAZ were obtained. They were washed with cold water and dried in the air. The largest crystal isolated was (1.5cm x 1.5cm x 0.2cm). Anal. Calcd for NINAZ: C, 20.68; H, 5.79; N, 28.14. Found: C, 20.67; H, 5.79; N, 28.16.

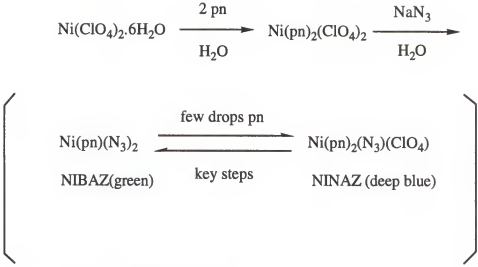

Scheme 3-1. Formation of NINAZ.

Deuterium 1,3-diaminopropane In order to synthesize the deuterated NINAZ, we first need to synthesize 1,3-diaminopropane-d_{10}. The whole synthesis Scheme is as follows:

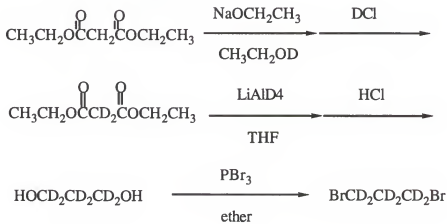

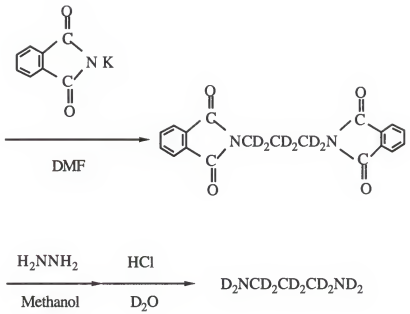

Scheme 3-2. The syntheses of 1,3-diaminopropane-d_{10}

Step 1

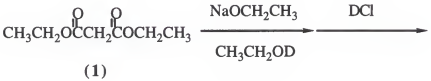

(1)

(2)

Sodium metal, 4.6g, was dissolved in 100 g CH_3CH_2OD in a 500ml 3-neck flask under argon, and reacted completely overnight. Diethyl malonate 60ml was added to the previous solution over about two hours, while the color of solution changed from white to clear. CH_3CH_2OD 40 ml was added to the clear solution, followed by 37 wt% DCl, added drop by drop until the pH of the solution reached 7. The solution was vaccum filtered on a

Buchner funnel to remove the solid, and the filtrate containing the desired product was kept. The product was purified by distillation under vaccum (around 10 torr), and the portion that distilled at 65° C was collected. ^1H NMR indicates around 90% conversion based on the ratio of the $\delta = 3.35$ ppm resonance (see Figure 3-2 and 3-3).

Step 2

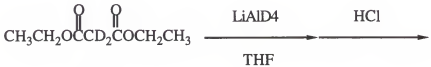

(**2**)

$HOCD_2CD_2CD_2OH$

(**3**)

$LiAlD_4$, 15g, was dissolved in 250 ml dry THF in a 3-neck 1000 ml round bottom flask, followed by dropwise addition of 32 ml (**2**). The whole process should be kept under argon and the temperature kept at 0°C. After the addition is complete, the system is refluxed (70° C) for four hours. A solution is made of 5 ml 12N HCl and 30ml H_2O in 200 ml THF, and 20 ml of this solution is added drop by drop to the previous solution, followed by 40ml water also added drop by drop with the system kept at 0°C. The color of the solution changes from gray to white. The solution was vaccum filtered on a Buchner funnel to remove the solid, and the filtrate containing the desired product was kept. The product was purified by distillation under vaccum (around 10 torr), and a 3.4 ml portion was collected at 90°C. The yield is 60%.

Figure 3-2. ^{1}H NMR spectrum of $CH_3CH_2O_2CCH_2CO_2CH_2CH_3$ **(1)**

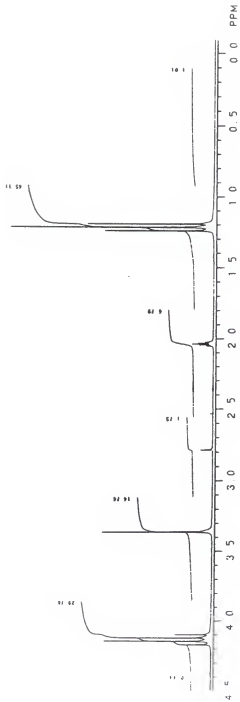
PPM
4.0
3.5
3.0
2.5
2.0
1.5
1.0
0.5
0.0
29.74
14.26
6.28
3.23
65.31
1.01

Figure 3-3. ^{1}H NMR spectrum of $CH_3CH_2O_2CCD_2CO_2CH_2CH_3$ **(2)**

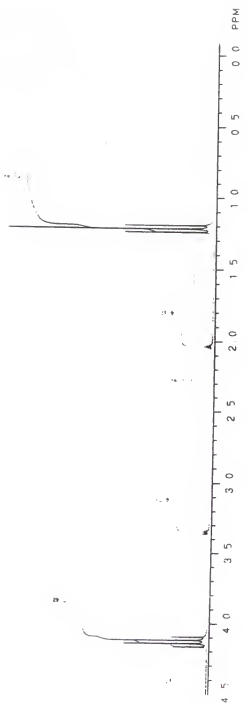
PPM
0 0
0 5
1 0
1 5
2 0
2 5
3 0
3 5
4 0
4 5

Step 3

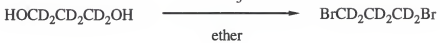

(**3**) (**4**)

A solution of 10ml (0.138 mole) of 1,3-propanediol in 50 ml of dry ether was stirred in a dry atmosphere and cooled to 0°C. Then there was added dropwise 9.39 ml (0.1 mole) of phosphorus tribromide. Cooling was continued so as to maintain the temperature below 5° C during the addition. After the addition was completed, the solution was allowed to warm to room temperature and stand for 30 hours. After the reaction mixture had been poured onto crushed ice, the organic layer was separated, washed with water and with 10% sodium carbonate solution, then dried over anhydrous potassium carbonate and fractionally distilled under vaccum (about 10 torr). The principal fraction was composed (**4**) 4ml (65% yield) collected at 45°C.

Step 4

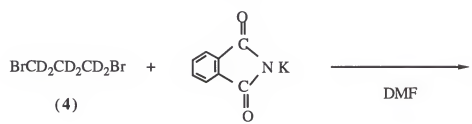

(**4**)

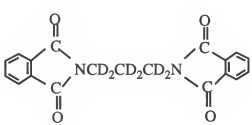

(**5**)

A mixture of potassium phthalimide (20.37g, 0.11mole) and (**4**) (5 ml, 0.049 mole) in 100 ml dry DMF was heated at 55°C for 2 hours with stirring under an argon atmosphere. 170 ml chloroform was added to the mixture followed by 500 ml water. The organic layer was separated and the water layer was extracted with 100 ml chloroform. The combined organic layer was washed with 100 ml 3N NaOH, then 100 ml water. The new combined organic layer was dried over sodium sulfate, and then solvent was evaporated under reduced pressure. A lot of white solid (**5**) (12.84 g, 78.4% yield) was obtained, after washing with cold ether and drying in the air.

Anal. Calcd for (**5**): C, 68.26. N, 8.38. Found: C, 68.11. N, 8.35.

Step 5

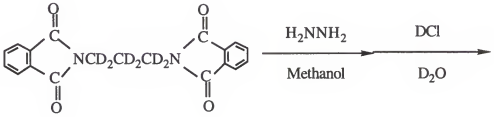

(**5**)

$D_2NCD_2CD_2CD_2ND_2$

(**6**)

The phthalimide (**5**) (12.5g, 0.037 mole) was pulverized and suspended in 170 ml of methanol and 3 ml (0.094 mole) of a 1M solution of hydrazine hydrate in 95% methanol was added. After refluxing for 30 minutes, the suspension was stored overnight and then concentrated to dryness under vacuum. The residue was then stirred in 80ml of 6N DCl, refluxed 30minutes, filtered, and the liquid phase was kept at 0°C for 20 minutes. The solution was evaporated under water aspiration. After evaporating the solvent, 0.035 mole (5.15g) ($H_2NCD_2CD_2CD_2NH_2$)·2HCl (**5-1**) was obtained. 3.5g NaOH and 5.15g (**5-1**)

were ground with 10 ml D_2O, then distilled under 1 atm. The portion above 104 °C was collected (2.24ml (**6**)).

NINAZ-d_{20} The same procedure was followed as described for the synthesis of hydrongenated NINAZ. The only difference is the use of 1,3-diaminopropane-d_{10} in place of 1,3-diaminopropane.

Ultra-fine Powder NINAZ

The ultra-fine powder NINAZ sample was prepared by Nelson Bell in the Department of Materials Science by mixing ZrO_2(s) and crystalline NINAZ in circular mill for 3-4 hours. After that, a 400 mesh (diameter = 38 μm) metal screen was used to filter NINAZ particles with size smaller than 38 μm.

Magnetic Measurements

The magnetic measurements of NINAZ were performed in collaboration with our physics colleaques Kim et al.[55] and recent contributions from Garret E. Granroth. Measurement were made down to 1.8 K using a commercial magnetometer which provided absolute $\chi(T)$ values, Figure 3-4 . Low-temperature, low-frequency χ(60 mK $\leq T \leq$ 4.2 K) work utilized standard mutual inductance techniques, and the background contribution has been measured and subtracted from the data. Absolute $\chi(T)$ values were obtained by normalizing the data to the results of the magnetometer work in the overlapping temperature region.

Figure 3-4. The χ(T) data for NINAZ in a 1.0 kG magnetic field is shown. The inset shows the low temperature results.[55]

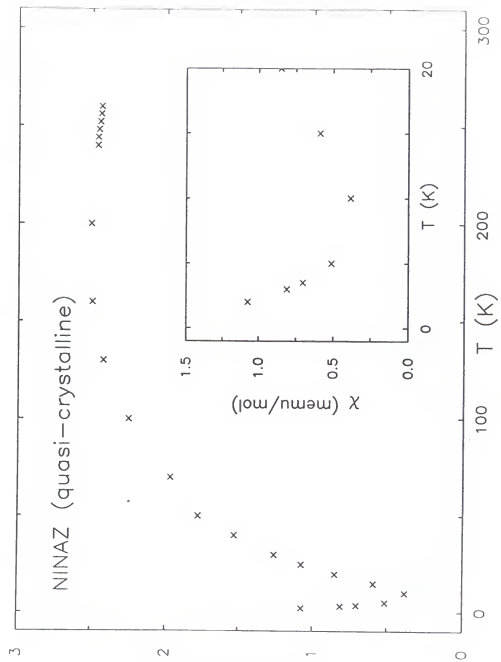
NINAZ (quasi-crystalline)
χ (memu/mol)
T (K)
χ (memu/mol)
T (K)

ESR Measurements

Electron spin resonance spectra were recorded by use of a Bruker ER-200 spectrometer. Samples were mounted on a cut edge of a quartz rod and rotation was achieved using a home-built goniometer. Samples were cooled using an Oxford Instruments cryostat. The temperature was measured with a AuFe/Ch thermocouple.

Elemental Analysis

The NINAZ elemental analysis was completed by Dr. Monica Escobar. For the elemental analysis reported here, two samples were prepared for the measurements. One was 52 mg powder NINAZ (A), the other was 52 mg ultrafine powder sample (B). Samples were dissolved in 25 ml Millipore Water. The following elements were determined using nebulization inductively coupled plasma mass spectrometry using the multiplier detector. Fe was determined using electrothermal vaporization inductively coupled plasma mass spectrometry using the electron multiplier detector. Because the Ni signal (mass 58, 60, 61, 62 and 64) in the mass spectrum was so large, (offscale on the Farady detector), it interfered with the detection of Co (mass 59). Ni peaks also interfered with the detection of the most abundant Cu and Zn isotopes, limiting sensitivity. From the following data, we believe the NINAZ powder and ultrafine powder samples are pure, there are only trace amounts of extrinsic impurities in both samples.

Element	Conc. in Soln.	Conc. in Solid	Comments
^{27}Al	< 8 ppb	< 4 ppm	Blank-limited
^{55}Mn	< 50 ppb	< 20 ppm	Blank-limited
^{59}Co	-	-	Could not be determined
^{65}Cu	A: 200 ppb B: 300 ppb	A: 100 ppm B: 160 ppm	
^{66}Zn	< 20 ppb	< 10 ppm	Blank-limited
^{56}Fe	A: 20 ppb B: 50 ppb	A: 9 ppm B: 24 ppm	

Results and Discussion

NINAZ Structure

When we tried to idenfiy our NINAZ crystal structure, possibly the crystal is twin, we were unable to obtain the good goodness of fit of our crystal. Our result was similar to the Gadel et al.[59] The structure of NINAZ was characterized by Gadet et al.[59] Perspective views of the chain and of a mononuclear $[Ni^{II}(pn)_2(N_3)_2]$ unit are presented in Figure 3-5 and Figure 3-6, respectively. The structure consists of cationic polymeric chains of bis(1,3-propanediamine) nickel(II) bridged by an azido ligand in a 1,3 coordination mode. The chains are neutralized by perchlorate ions. The intrachain Ni-Ni distance is 5.849 Å and the interchain Ni-Ni distance is 7.58 Å. Each nickel(II) ion displays a distorted octahedral coordination, being linked to four nitrogen atoms of two (1,3-propanediamine) ligands, which are disordered according to their thermal parameters, and two nitrogen atoms from the two aza ligands in the apical sites. Each 1,3-propanediamine-nickel ring

Figure 3-5. View perpendicular to the c axis of a portion of the Ni chain in NINAZ. Nickel chains are separated by perchlorate counterions.[59]

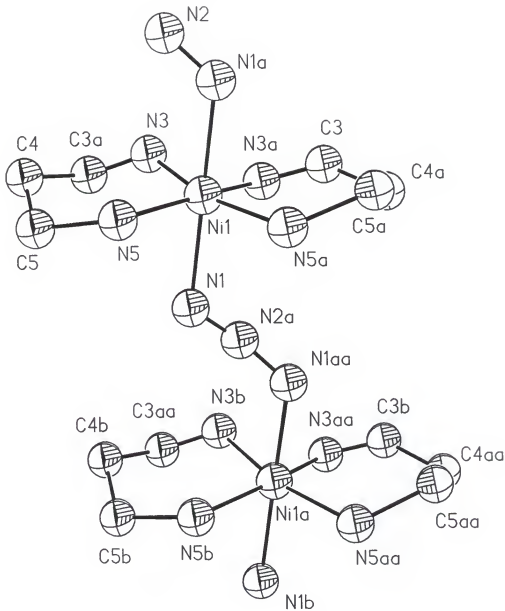
N2
N1a
N3
C4
C3a
N3a
C3
C4a
Ni1
C5a
C5
N5
N5a
N1
N2a
N1aa
N3b
C4b
C3aa
N3aa
C3b
C4aa
Ni1a
C5aa
C5b
N5b
N5aa
N1b

Figure 3-6. Packing diagram for NINAZ viewed along the c axis showing the separated nickel chains. Intrachain Ni-Ni distances are 5.849 Å, while the interchain distance is 7.58 Å.[59]

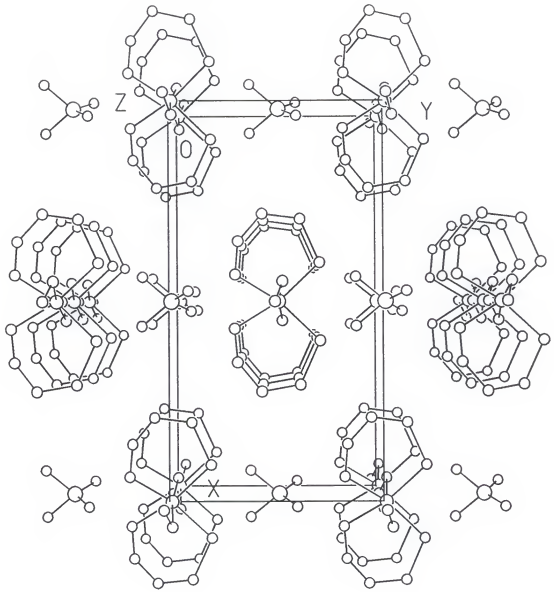
Z
O
Y
X

displays a typical chair conformation with the C(4) and Ni atoms out of the plane defined by the remaining four atoms.

Haldane Gap in NINAZ-d_{20}

Our collaborators, Dr. A. Zheludev et al.[60] measured the Haldane gap of NINAZ-d_{20} using the inelastic neutron scattering method at Brookhaven National Laboratory. Accordimg to their results, the Haldane gap energy is measured as approximately 3.75 meV.[60]

Magnetic Susceptibility

We have studied the $\chi(T \geq 1.8\ K)$ behavior of single-crystal NINAZ. In Figure 3-4, the increase of $\chi(T)$ below 10 K is difficult to eliminate and may due to the presence of end-chain effects. These results are consistent with the work of other researchers.[59] The single crystal was aligned with the magnetic field parallel to the Ni-chain axis. After the run, the sample had a light blue color and tended to break into small pieces very easily. This transformation arises from a shattering of the original single-crystal at a temperature of around 260 K and has been studied by Gadet et al.[59] These workers have shown that NINAZ experiences a reversible structural transition in this temperature range. We have been able to follow the transition in our $\chi(T)$ work, and our data agree with those of Gadet et al.[59] To date, we have not been able to cool through this transition without shattering the initial single-crystal. Therefore, in this chapter, we refer to our shattered specimens as poly-crystalline. At the end of one run, a poly-crystalline sample was pulverized with a pestle and mortar. The resultant material was pressed into a pellet and measured. The results, Figure 3-7, are nearly identical to the data obtained with the poly-crystalline starting

Figure 3-7. χ(60 mK $\leq$ T $\leq$ 12 K) of NINAZ and the Curie-Weiss fit for the same temperature range. The large boxes help show the overlapping region.[55]

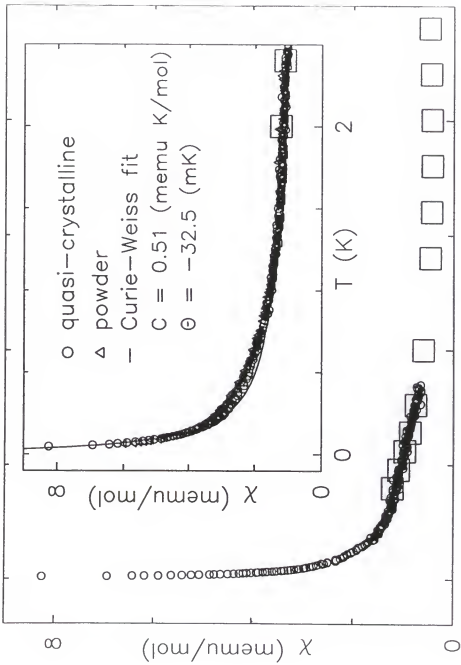
χ (memu/mol)
8
0
0
5
T (K)
10
o quasi-crystalline
Δ powder
– Curie-Weiss fit
C = 0.51 (memu K/mol)
Θ = −32.5 (mK)
χ (memu/mol)
8
0
0
T (K)
2

materials. A study of the powder suggests an average particle size of about 10 μm. In Figure 3-7, the $\chi(T \leq 2.0K) \leq 30$memu/mol data for two samples are shown. There are no differences between the two samples. Below 1.5 K, a large increase in the susceptibility has been observed in quasi-single crystalline and powdered samples. The results are interpreted in terms of the presence of end-chain spins. The result of a Curie-Weiss fit to the low-temperature tail is $\chi(0) = 1.02 \pm 0.02$ memu/mol, $C = 0.51 \pm 0.01$ memu K/mol and $\theta = -32.5 \pm 2.5$ mK. If the Curie tail is due solely to end-chain effects, we calculate that the chains are about 2700 Ni-spins long with a Ni-Ni spacing of 5.8 Å, yielding a typical chain length of about 0.9 μm. Figure 3-8, shows $\chi(T)$ vs T for NINAZ for two powder samples with different particle size. The χ vs T plot for the ultra-fine powder sample, figure 3-8, shows a smaller S = 1 contribution at high temperatures and a larger S = 1/2 contribution at low temperatures. Below 10 K in figure 3-9, the results are interpreted in terms of the presence of end-chain spins. The result for the ultra-fine powdered sample of the Curie-Weiss fit is $C = 15.91 \pm 0.83$ memu K/mol, $\theta = 0.043 \pm 0.085$ mK. If the Curie tail is due to end-chain effects, we calculate that the chains are about 56 Ni-spins long with a Ni-Ni spacing of 5.8 Å, yielding a typical lengh of about 36 nm.

ESR Result

In Figure 3-10 and Figure 3-11, we show the ESR signals of the same amount (64 mg) of powder and ultrafine powder samples of NINAZ at 4 K. The intensity of the spectrum for the ultrafine sample is more intense than that for the powder sample. This indicates that there are more S = 1/2 spins in the ultrafine sample than the powder samples. We also ran temperature-dependent ESR for the ultrafine and powder samples. In both samples, the signal could be seen below 15 K. When the temperature decreases, the signals become more intense in both samples (see Figure 3-12 and Figure 3-13). In the single crystal NINAZ, we recorded orientation-dependent ESR at 4K. When the magnetic

Figure 3-8. $\chi(T)$ vs T for NINAZ in two powder samples with different particle size.

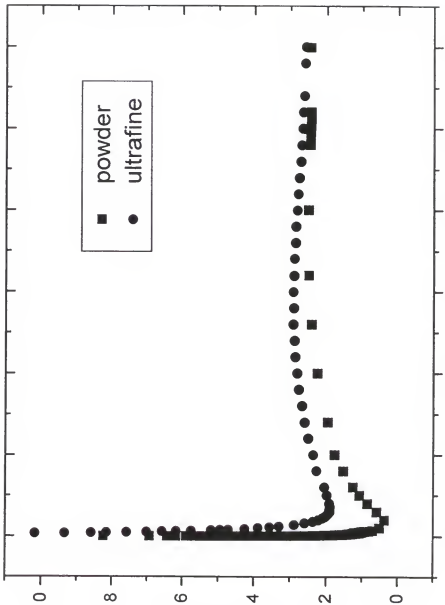
powder
ultrafine
χ (memu/mol)
T (K)
0
2
4
6
8
10
0
50
100
150
200
250
300

Figure 3-9. χ(60 mK $\leq$ T $\leq$ 12 K) for the ultrafine sample and the Curie-Weiss fit of the tail.

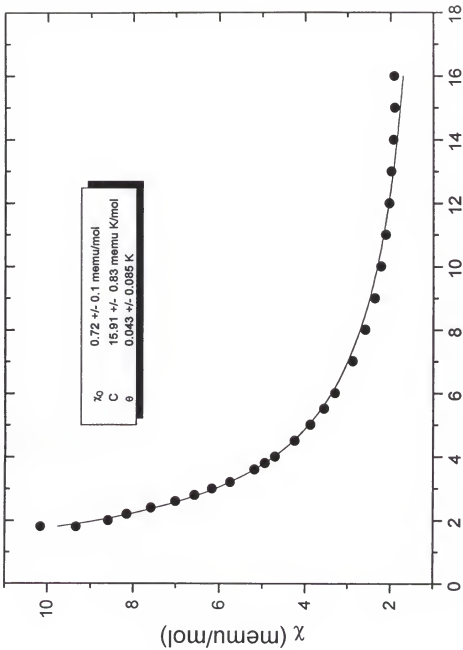
χ (memu/mol)
T (K)
χ0 0.72 +/- 0.1 memu/mol
C 15.91 +/- 0.83 memu K/mol
θ 0.043 +/- 0.085 K
0
2
4
6
8
10
12
14
16
18

Figure 3-10. EPR spectra for the ultrafine and powder NINAZ at 4 K.

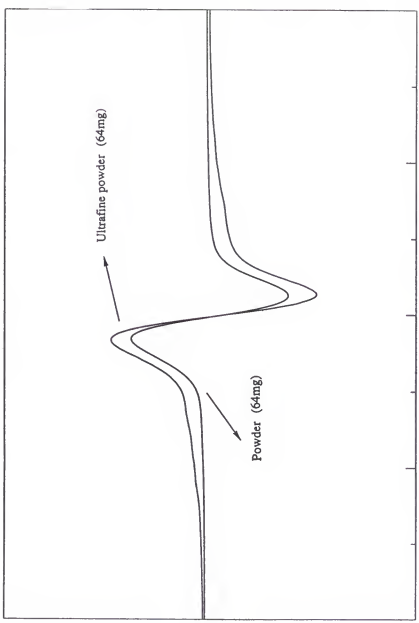
Ultrafine powder (64mg)
Powder (64mg)
2727
2902
3077
3252
3427
Magnetic Field (Gauss)

Figure 3-11. ESR spectrum for the ultrafine, powder and crystal NINAZ at 4 K.

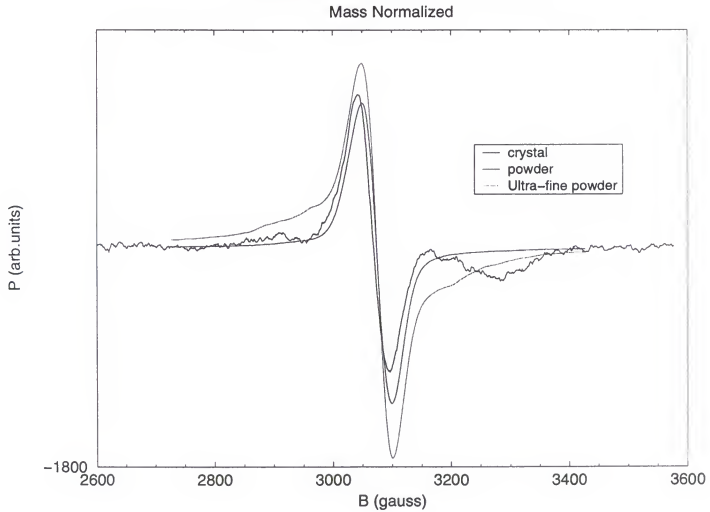
Sample comparison NINAZ
Mass Normalized
crystal
powder
Ultra–fine powder
P (arb.units)
–1800
2600
2800
3000
3200
3400
3600
B (gauss)

Figure 3-12. EPR spectrum for the powder NINAZ at 4, 7, and 11 K.

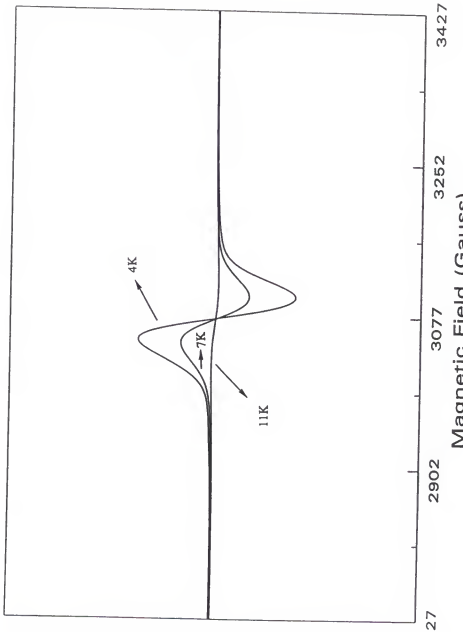
4K
7K
11K
2727
2902
3077
3252
3427
Magnetic Field (Gauss)

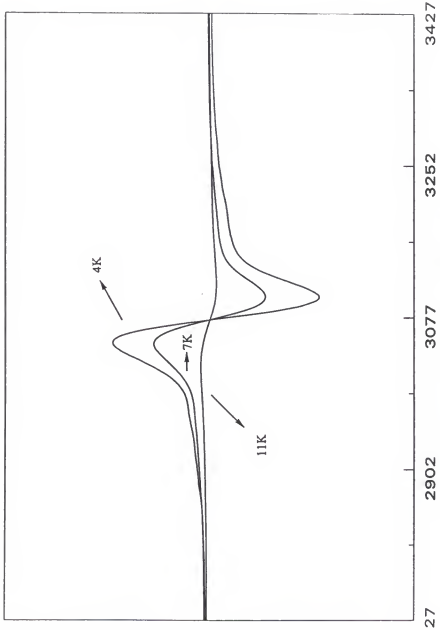
4K
7K
11K
2727
2902
3077
3252
3427
Magnetic Field (Gauss)

field is parallel the nickel chain, the $g_{//}$ value is 2.156. When the magnetic field is perpendicular to the nickel chain, the $g_{\perp}$ value is 2.165(see Figure 3-14). The g-value is nearly isotropic.

Conclusions

From the magnetic susceptibility measurements and ESR results, the ultra-fine NINAZ has stronger S = 1/2 character than that in powder NINAZ sample. Making assumptions about end-chain spins, i.e. $g \cong 2$ and S = 1/2, the C value given by the fit suggest a chain length of $\cong$ 56 Ni-spins in ultra-fine NINAZ and $\cong$ 2700 Ni-spins in powder NINAZ.

Figure 3-14. EPR spectrum for the single crystal NINAZ.

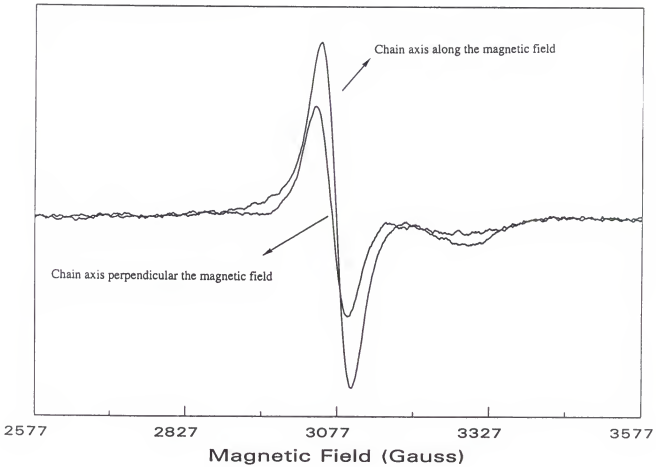
Chain axis along the magnetic field
Chain axis perpendicular the magnetic field
2577
2827
3077
3327
3577
Magnetic Field (Gauss)

CHAPTER 4
DICATION SALTS OF THE ORGANIC DONOR
BIS(ETHYLENEDITHIO)TETRATHIAFULVALENE#

The organic π-donor bis(ethylenedithio)tetrathiafulvalene (BEDT-TTF) is the basis of a large number of conducting and superconducting cation-radical molecular solids.[25] Conductivity in these materials occurs via the donor-ion network that results from close intermolecular contacts in the solid. The donor-ion networks are often stacks or sheets that are separated by the counterions.[63] The most common route to pure crystalline samples of conducting cation-radical salts is through electrochemical oxidation of the donor in the presence of an appropriate counterion. Salts are generally formed where the oxidation state of the donor ranges from +1/2 to +1, and all of the current superconducting examples have donor oxidation states of +1/2 or +2/3.[64]

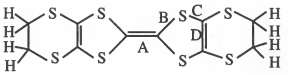

BEDT-TTF

The following experimental results have already been published in ref. 61 and 62.

In principle, solids where the donor has a nonintegral oxidation state between +1 and +2 could also be conductors with potentially interesting properties. Such examples would have degrees of band filling different from the presently known materials. In practice, however, there are only a few examples of BEDT-TTF cation-radical salts where the degree of oxidation is greater than +1. If high-oxidation state salts are to be prepared by electrocrystallization, methods need to be developed to stablize the donor cations in solution and prevent precipitation of the more common "low-oxidation state" salts. In this chapter, we describe the preparation of dication salts of BEDT-TTF where the donor is first chemically oxidized to the monocation followed by electrochemical oxidation to the dication. Tetrafluoroborate and perchlorate salts of the BEDT-TTF dication have been isolated, and their crystal structures are described. While optical reflectivity shows that these dication salts are not conducting, the route used to isolate them appears to be general and could be used to pursue cation-radical salts of BEDT-TTF and related donors with nonintegral oxidation states greater than +1.

Experimental Section

Materials

BEDT-TTF was synthesized by the method of Larsen and Lenoir.[65] Tetra-n-butylammonium tetrafluoroborate, tetraethylammonium perchlorate, and tetra-n-butylammonium perchlorate were obtained from Southwestern Analytical Co. (Austin, TX) and then twice recrystallized from an ethyl acetate-pentate mixture. Benzonitrile (C_6H_5CN, 99%) and chloroacetyl chloride ($ClCH_2COCl$, 98%) were purchased from Aldrich Chemical Co. (Milwaukee, WI). Benzonitrile was purified by distillation, and chloroacetyl chloride was used without further purfication. Carbon disulfide (CS_2) was purchased from Fisher Scientific Co. (Pittsburg, PA) and used without further purification.

Synthesis Scheme

In our method to isolate the high oxidation state BEDT-TTF salt, the first step is to use a chemical oxidant to oxidize BEDT-TTF following:

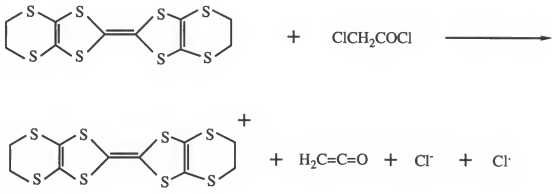

Scheme 4-1. Donor oxidation in solution to monocation by chloroacetychloride (10% by volume) in benzonitrile.

After we obtain BEDT-TTF$^+$ in solution, electrooxidation is used to give the dication. Electrocrystallization is performed in an H-cell (Figure 4-1).

BEDT-TTF$(BF_4)_2$ (1) *Method 1* : This method was completed by our former group member Glênnison F. de Oliveria. BEDT-TTF (10 mg) was placed in the working electrode arm of a two-electrode H-cell containing a total of 2 mL of 2.5 x 10^{-2} M tetrabutylammonium tetrafluoroborate in 10% $CS_2/ClCH_2COCl$. A constant current density of 1 $\mu A/cm^2$ was maintained at room temperature between the platinum working and counter electrodes that were separated by two glass frits. After a few days, needles could be seen on the electrode surface and at the bottom of the H-cell. Small blue needles were collected after 28 days. *Method 2* : BEDT-TTF (7 mg) was dissolved in 36 mL of 1.0 x 10^{-2} M tetrabutylammonium tetrafluoroborate in 10% $ClCH_2COCl$/benzonitrile and oxidized in an H-cell as described above. The cells were maintained at room temperature

Figure 4-1. Cell and electrodes typically used in the electrocrystallization of cation-radical salts.[66]

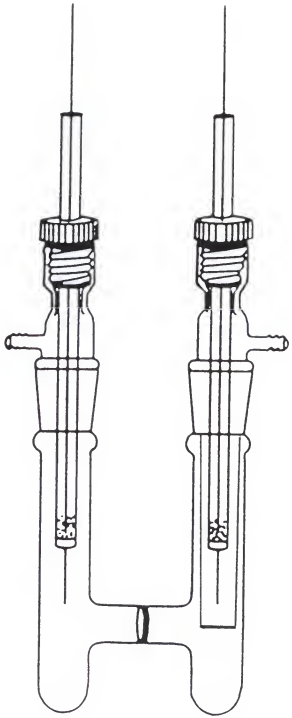

with a constant current density of 1.5 $\mu A/cm^2$. As above, crystals were observed within a few days and were collected after 21 days.

BEDT-TTF$(ClO_4)_2$ (2) Using method 1, described above with 6 x 10^{-2} M tetraethylammonium perchlorate as electrolyte, crystals were isolated as thin blue plates. Crystals were also prepared according to method 2 with 1.0 x 10^{-2} M tetrabutylammonium perchlorate as electrolyte.

Crystallographic Data Collection and Structure Determination

The X-ray measurement was completed by Dr. Khalil A. Abboud. X-ray data for **1** and **2** were collected at room temperature on a Siemens R3m/V diffractometer equipped with a graphite monochromator utilizing MoK_α radiation. In each case, 50 reflections with $20.0^\circ \leq 2\theta \leq 22.0^\circ$ were used to refine the cell parameters. Four reflections ($0\bar{1}\bar{3}$, $12\bar{3}$, 113, $2\bar{1}1$) for **1**, and ($02\bar{1}$, $1\bar{3}5$, 011, $01\bar{1}$) for **2**, were measured every 96 reflections to monitor instrument and crystal stability (maximum correction on I was < 1 %). Absorption corrections were applied based on measured crystal faces using *SHELXTL plus* .[41]

The structures were solved by direct methods in *SHELXTL plus* [41] from which the locations of the non-H atoms were obtained. The structures were refined in *SHELXTL plus* using full-matrix least squares. The non-H atoms were treated anisotropically. In **1**, the CH_2CH_2 units of the cation are disordered (site occupation factors were refined to 0.64 for the C4-C5 unit and 0.36 for the C4'-C5' unit with an e.s.d of 0.02). The disordered H-atoms were calculated in idealized positions and their isotropic thermal parameters fixed at 0.08. In **2**, the CH_2CH_2 units of the cation are also disordered (site occupation factors were refined to 0.65 for the C4-C5 unit and 0.35 for the C4'-C5' unit with an e.s.d of 0.03). Each of the disordered CH_2 units has a H-atom of full occupancy (H4 or H5, common to both disordered units) and a disordered H-atom (H4a and H4a' on C4 and C4', respectively; H5a and H5a' on C5 and C5', respectively). H4a' and H5a' were calculated

in idealized positions and their isotropic thermal parameters fixed at 0.08. H4, H5, H4a and H5a were refined without any constraints. There were 146 and 162 parameters for **1** and **2**, respectively, were refined and $\Sigma\omega(|F_o| - |F_c|^2$ was minimized; $\omega = 1/(\sigma|F_o|)^2$, $\sigma(F_o) = 0.5kI^{-1/2}\{|\sigma(I)|^2 + (0.02I)^2\}^{1/2}$, I(intensity)= (I_{peak} - $I_{background}$)(scan rate), and $\sigma(I) = (I_{peak} + I_{background})^{1/2}$ (scan rate), k is the correction due to decay and Lp effects, 0.02 is a factor used to down weight intense reflections and to account for instrument instability. The linear absorption coefficient was calculated from values from the *International Tables for X-ray Crystallography* .[42] Scattering factors for non-hydrogen atoms were taken from Cromer & Mann [43] with anomalous-dispersion corrections from Cromer & Liberman ,[44] while those of hydrogen atoms were from Stewart, Davidson & Simpson .[45]

Optical Measurement

Measurements on the solid were completed by Dr. Manuel A. Quijada in Department of Physics. Two crystals with large enough surface area (1 x 1 mm^2) were selected for optical measurements. The principal optical axes in the (001) face were identified by observing the extinction point when rotating the sample under an Olympus (Tokyo, Japan) Model BHM microscope with crossed polarizers. The a and b axes in the crystal coincide with the directions of maximum optical anisotropy. Polarized reflectance along these two axes was measured in the frequency range 3000-32000 cm^{-1} using a Perkin-Elmer (Norwark, CT) monochromator. Each sample was mounted by fixing it onto a frame with a 1 mm diameter hole. A piece of Al-coated glass was mounted the same way as the sample and used as the reference. The surface of the sample was flat and smooth, giving a nearly specular reflectance. Transmittance of one sample was measured in the far- and mid-IR (100-4000 cm^{-1}) using a fast-scanning Bruker (Billerica, MA) IFS-113V Fourier interferometer. Solution UV-vis spectra were obtained with a Perkin-Elmer 330 spectrophotometer.

Results and Discussion

Synthesis and Structure

The BEDT-TTF dication salts were isolated during attempts to define conditions where small molecules can be purposefully incorporated into cation-radical salts to form ternary structures. Incorporation of small neutral molecules into the lattice represents a way to vary donor ion packing by changing the unit cell volume. Previously, a former group member, Marvin B. Clevenger, had isolated a salt, $(BEDT\text{-}TTF)_2PF_6 \cdot ClCH_2COCl$, where the BEDT-TTF packing is different than observed in other PF_6^- salts and is similar to that seen in the conductor $\beta'\text{-}(BEDT\text{-}TTF)_2AuBr_2$.[35] The dication salts were initially isolated from a standard constant-current electrocrystallization cell using a solvent mixture of 10% CS_2 in $ClCH_2COCl$ and have since been reproduced using a 10% $ClCH_2COCl$/benzonitrile solvent mixture according to the conditions described in the Experimental Section. In all cases, the donor ion is slowly oxidized by the solvent medium to form a solution containing the BEDT-TTF monocation. The dication is then formed electrochemically and is isolated at the anode by crystallization with the electrolyte anion. Optical spectroscopy shows that BEDT-TTF is slowly oxidized by $ClCH_2COCl$. Figure 4-2 compares the optical spectrum of a 6.75×10^{-4} M solution of BEDT-TTF in 1,1,2-trichloroethane with the spectrum from the same solution containing a 2-fold excess of $ClCH_2COCl$. Bands between 400 and 600 nm are intramolecular transitions of the BEDT-TTF monocation.[67] The band at 960 nm is an intermolecular charge-transfer band resulting from the formation of dimers in solution.[68]

$BEDT\text{-}TTF(BF_4)_2$ (**1**) forms as small six-sided needles and slowly degrades in air over a period of days while $BEDT\text{-}TTF(ClO_4)_2$ (**2**) forms as very thin hexagonal plates and is stable in air for several months. Both salts exhibt a blue tint. The two salts are isostructural, crystallizing in the monoclinic space group P21/n. Crystallographic data for

Figure 4-2. Optical spectra of 6.75 x 10^{-4} M BEDT-TTF in 1,1,2-trichloroethane (solid line) and in the same solution containing a 2-fold excess of $ClCH_2COCl$ (dashed line). Bands between 400 and 600 nm are localized transitions of the BEDT-TTF monocation, while the band at 960 nm is an intermolecular transition resulting from the formation of dimers in solution.[61]

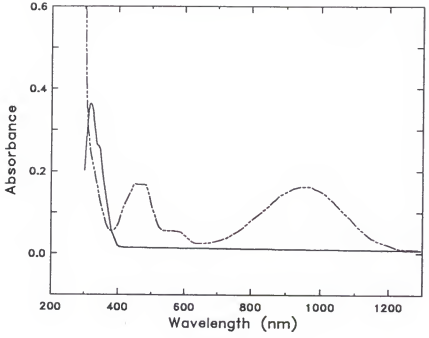
0.6
0.4
0.2
0.0
Absorbance
200
400
600
800
1000
1200
Wavelength (nm)

both salts are presented in Appendix Table B-1. Atomic coordinates are listed in Appendix Table B-2, and bond lengths and angles are presented in Appendix Table B-3 for both **1** and **2**. Figure 4-3 shows a packing diagram for **1** including both anions and cations. All BEDT-TTF dications are equivalent and surrounded by six counterions in a distorted octahedron. Intermolecular overlap between donor molecules is weak, and the nearest intermolecular S-S contacts are 3.620 Å in **1** and 3.621 Å in **2** from an inner ring sulfur to an outer ring sulfur on adjacent molecules.

Oxidation of BEDT-TTF results in an increase in the C-C bond lengths and a decrease in the C-S bond lengths of the fulvalene core.[75] This is consistent with MO calculations that show the BEDT-TTF HOMO is predominately contained with the fulvalene core and has nodes at the C-S bonds.[76] The bond lengths of the TTF core of **1** and **2** are listed in Table 4-1 and are compared to the bond lengths in a series of salts with different BEDT-TTF formal oxidation states. The central C-C bond, in the dication salts is long, 1.430 Å in **1** and 1.439 Å in **2**, with the latter being the longest central C-C bond observed in a BEDT-TTF cation-radical salts. The C-S bonds in **1** and **2** are shorter than the comparable bonds in salts where the BEDT-TTF oxidation state is ≤ 1.

Donor ion bond lengths have been used to assign oxidation states in charge transfer salts and mixed valent cation-radical salts of BEDT-TTF.[77] Characterization of BEDT-TTF dication salts will now help extend these correlations to salts with oxidation states greater than +1. For example, in Table 4-1, bond-length correlations are used to confirm the coexistence of BEDT-TTF^{+} and BEDT-TTF^{2+} ions in the mixed-valent salts (BEDT-TTF)$_3$($ZnCl_4$)$_2$ [72] and (BEDT-TTF)$_3$($MnCl_4$)$_2$.[73] The central C-C bond is most sensitive to changes in oxidation state,[78] and a bond length of 1.438 Å on one donor molecule in (BEDT-TTF)$_3$($ZnCl_4$)$_2$ shows that the BEDT-TTF dication is present in this salt, coexisting with BEDT-TTF monocations where the central C-C bond length is 1.378 Å.

Figure 4-3. Crystal structure showing the molecular packing of **1**. The crystal structure of **2** is isostructural with **1**.[61]

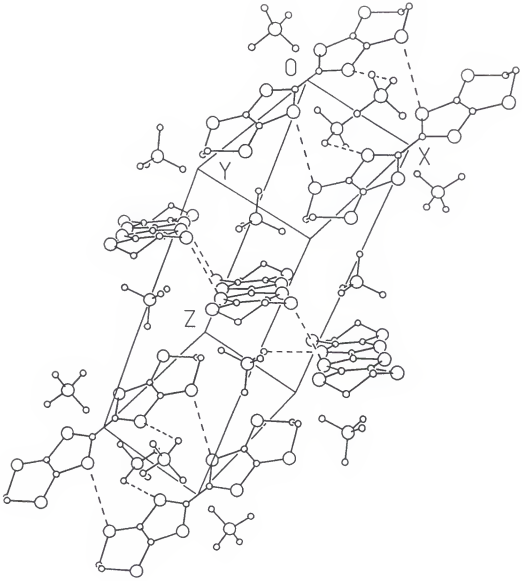
O
Y
X
Z

Table 4-1. Bond Lengths[a] of the TTF core in BEDT-TTF$^{+\rho}$ Cation-Radical Salts[61]

Compound	ρ	Bond Length (Å)			
		A[b]	B	C	D
BEDT-TTF[c]	0	1.312(12)	1.757(7)	1.754(8)	1.332(7)
$(BEDT\text{-}TTF)_2ClO_4(TCE)_{0.5}$[d]	1/2	1.359	1.729	1.755	1.294
$(BEDT\text{-}TTF)_3(ClO_4)_2$[e]	2/3	1.366(7)	1.731(7)	1.743(5)	1.345(9)
ε-(BEDT-TTF)ClO_4[f]	1	1.390(7)	1.721(3)	1.738(4)	1.365(6)
$(BEDT\text{-}TTF)_3(ZnCl_4)_2$[g]		1.378(7)	1.721(6)	1.738(6)	1.360(6)
BEDT-TTF$(ClO_4)_2$	2	1.439(4)	1.683(3)	1.716(3)	1.379(5)
BEDT-TTF$(BF_4)_2$		1.430(4)	1.687(3)	1.717(3)	1.369(4)
$(BEDT\text{-}TTF)_3(ZnCl_4)_2$[g]		1.438(7)	1.680(6)	1.710(6)	1.369(7)
$(BEDT\text{-}TTF)_3(MnCl_4)_2$[h]		1.431	1.685	1.715	1.361
$(BEDT\text{-}TTF)_5Hg_5Br_{11}$[i]		1.43	1.68	1.71	1.34
$(BEDT\text{-}TTF)_5Hg_5Br_{11}$[i]		1.41	1.69	1.72	1.37

Table notes.
a. Bond lengths are averaged assuming D_2h symmetry for the TTF core.
b. Bonds refer to those labelled on the structure shown in the text.
c. Reference 69. d. Reference 70. e. Reference 68. f. Reference 71. g. Reference 72.
h. Reference 73. i. Reference 74.

Optical Properties

Transmittance spectra for **2** were measured from 100 to 3000 cm^{-1} in two polarizations. There is no evidence for low-frequency metallic behavior in the IR. This is not surprising as the donor HOMO is fully oxidized in the dication leaving no partially filled levels in the solid. In addition, the crystal structure shows that the donor molecules are essentially isolated from one another, and intermolecular interactions are weak. Figure 4-4 shows the room-temperature reflectance parallel to the a and b axes of **2** from 200 to 2900 nm. The spectra were identical for two samples, and only one set of data is shown. Figure 4-5 shows the optical absorption coefficient obtained from Kramers-Kronig analysis.[94] Two bands strongly polarized along the b axis are observed in the near-IR near 855 nm (11700 cm^{-1}) and 714 nm (14000 cm^{-1}). These transitions are probably localized excitons and not charge-transfer transitions as are sometimes observed in BEDT-TTF cation-radical salts.[80] The direction of closest contact between BEDT-TTF ions is along the a axis and any intermolecular transitions are expected to be polarized along this direction. The long axis of the BEDT-TTF ions projects primarily along the b direction suggesting that the 855 and 714 nm bands are localized excitons polarized along the long axis of the molecule. Similar transitions are observed in monocation salts although at higher energy.[80] Some intensity is observed in the a polarization as a result of the monoclinic space group. The band at 323 nm (31000 cm^{-1}) is nearly isotropic in the ab plane, and the high energy sugests this band is also an intramolecular excitation.

Conclusions

Dication salts of the organic donor BEDT-TTF have been isolated by first stabilizing a solution of the monocation followed by electrochemical oxidation and crystallization as the BF_4^- and ClO_4^- salts. Optical spectroscopy shows no evidence for metallic behavior in these salts which is to be expected if the singly degenerate HOMO is

Figure 4-4. Optical reflectivity data from **2** polarized along the a and b axes. Lorentz fits to the data are shown as the dashed lines.[79] Interference fringes are observed at low energy where the thin crystal becomes transparent. Squares and triangles are single-bounce reflectance values.[79]

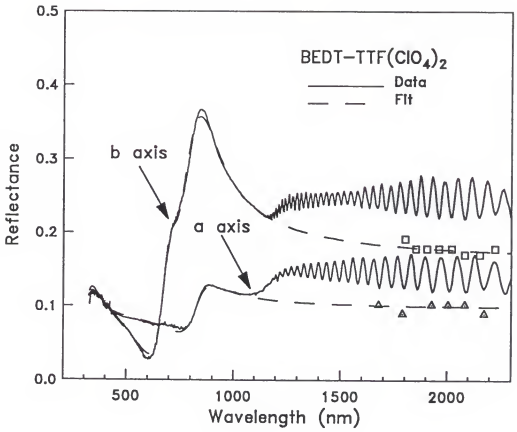
BEDT–TTF(ClO4)2
Data
Fit
b axis
a axis
Reflectance
Wavelength (nm)
0.0
0.1
0.2
0.3
0.4
0.5
500
1000
1500
2000

Figure 4-5. Polarized absorption coefficient of **2**, obtained from Kramers-Kronig analysis of the data in Figure 4-4.[79]

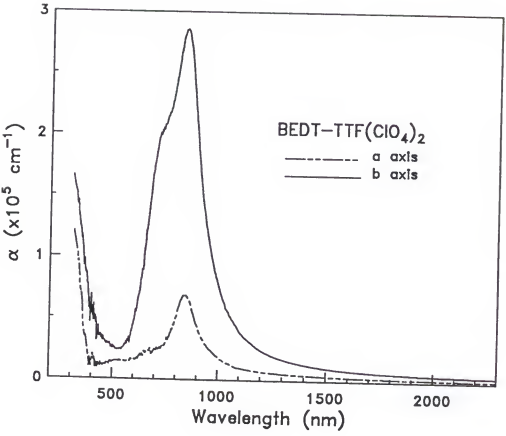
BEDT–TTF(ClO4)2
a axis
b axis
α (x10^5 cm^-1)
Wavelength (nm)
0
1
2
3
500
1000
1500
2000

completely oxidized. The method of preparation appears to be general, and could be used in attempts to prepare other examples of high-oxidation state cation-radical salts. Examples where the donor oxidation state is between +1 and +2 could be particularly interesting.

CHAPTER 5
STRUCTURE, MAGNETIC, OPTICAL, AND TRANSPORT PROPERTIES OF (BEDT-TTF)PF_6*

Introduction

In the preparation of cation-radical salts of BEDT-TTF the observation of different crystal morphologies is a common result. In order to vary the mode of BEDT-TTF packing in some cation-radical salts, we have tried to incorporate small molecules, such as $ClCH_2COCl$ and CS_2 into the crystal lattice. Previously, our former group member Marvin B. Clevenger[81] isolated a salt, (BEDT-TTF)$_2PF_6$·$ClCH_2COCl$, where the BEDT-TTF packing is different than observed in other PF_6^- salts and is smilar to that seen in the conductor β'-(BEDT-TTF)$_2AuBr_2$.[35,82] When we tried to incorporate CS_2 into the BEDT-TTF crystal lattice, instead of obtaing (BEDT-TTF)$_2PF_6$·CS_2 we isolated δ-(BEDT-TTF)PF_6, [96] ε-(BEDT-TTF)PF_6,[91] and (BEDT-TTF)PF_6*. The structures of the previously reported δ-(BEDT-TTF)PF_6 and (BEDT-TTF)PF_6* are similar. The only difference is that there are dimers of BEDT-TTF along the stacking axis in δ-(BEDT-TTF)PF_6 and there are no dimers in (BEDT-TTF)PF_6*.

The magnetic properties of organic radical salts is a topic of high interest which brings together many subfields of solid-state chemistry and physics. In the BEDT-TTF family, several types of electronic and magnetic phase transitions have been observed : superconductor to insulator [α-(BEDT-TTF)$_2(NH_4)Hg(SCN)_4$][83], metal to insulator

We have not yet decided an appropriate nomenclature for (BEDT-TTF)PF_6*

$[(BEDT\text{-}TTF)_2I_3]$[84], insulator to insulator $[\alpha'\text{-}(BEDT\text{-}TTF)_2Ag(CN)_2]$.[85] Most of the above structure types are 2:1 salts. The 1:1 donor-anion stoichiometry is relatively rare among BEDT-TTF salts containing monovalent anions, but has been observed in some anions system: $Ag_4(CN)_5^-$,[86] $AuBr_2Cl_2^-$,[87] BiI_4^-,[28] PF_6^-.[88] So far only Porter et al.[87] have researched the magnetic properties of 1:1 BEDT-TTF salts. They only reported ESR data from 300K to 100K, finding $(BEDT\text{-}TTF)AuBr_2Cl_2$ salt is a semiconductor which has no transition in this temperature range. $(BEDT\text{-}TTF)PF_6$* is the new form of 1:1 salt in the BEDT-TTF family. We will discuss the structure and physical properties of $(BEDT\text{-}TTF)PF_6$* further below.

One class of insulator to insulator transition seen in organic cation radical salts is a spin-Peierls transition. A spin-Peierls transition is a consequence of magnetoelastic couping between a one dimensional antiferromagnetic chain of localised spins and a three dimensional phonon, resulting in a temperature dependent lattice dimerisation to an alternating chain.[89] Of the many hypothetical examples of spin Peierls systems few have been properly characterised; those are the parent salt in the organic family $MEM\text{-}TCNQ_2$, (MEM=N-ethyl morpholinium, TCNQ = tetracyanoquinodimethanide)[90] and the inorganic-organic compound $TTF\text{-}M(X_2C_2(CF_3)_2)_2$, (TTF = tetrathiafulvalene, M = Cu or Au and X = S or Se).[91] In the BEDT-TTF family, $\alpha'\text{-}(BEDT\text{-}TTF)_2Ag(CN)_2$ [85] is the only salt to show a transition due to the spin-Peierls mechanism. In this chapter the characterization of $(BEDT\text{-}TTF)PF_6$* by several techniques is described, such as conductivity measurements as a function of temperature, crystal structure at room and 173 K, temperature-dependent optical measurement, magnetic susceptibity and electron spin resonance. The crystal behaves as a semiconductor at all temperatures and has an activation energy of 0.55eV. There is evidence for a structural phase transition at 250K. From the magnetic susceptibility and ESR measurement, there is a possibile spin-Peierls transition below 30 K.

Experimental Section

Materials

BEDT-TTF was synthesized by the method of Larsen and Lenoir.[65] Tetra-n-butylammonium hexafluorophosphate and dichloromethane (CH_2Cl_2, 99.6%) were purchased from Aldrich Chemical Co. (Milwaukee, WI). Tetra-n-butylammonium hexafluorophosphate was twice recrystallized from an ethanol. Dichloromethane was used without further purfication. Carbon disulfide (CS_2) was purchased from Fisher Scientific Co. (Pittsburg, PA) and used without further purification.

(BEDT-TTF)PF_6*, δ-(BEDT-TTF)PF_6, and ε-(BEDT-TTF)PF_6

BEDT-TTF (7 mg) was placed in the working electrode arm of a two-electrode H-cell containing a total of 33 mL of 1.0 X 10^{-2} M tetrabutylammonium hexafluorophosphate in 10% CS_2/CH_2Cl_2. A constant current density of 1.5 $\mu A/cm^2$ was maintained at room temperature between the platinum working and counter electrodes that were separated by two glass frits. We have observed that allowing air inside the cell and the use of undistilled solvent increases the yield of the (BEDT-TTF)PF_6* phase. After a few days, needles and plates could be seen on the electrode surface and at the bottom of the H-cell. Small black needles and plates were collected after 10 days.

Crystallographic Data Collection and Structure Determination

The X-ray measurement was completed by Dr. Khalil A. Abboud. The X-ray data of (BEDT-TTF)PF_6* were collected at room temperature and 173K on a Siemens diffractometer.

Room Temperature The X-ray data of (BEDT-TTF)PF_6* was collected at room temperature on a Siemens R3m/V diffractometer with a graphite monochromator utilizing M_oK_α radiation ($\lambda = 0.71073$ Å). In each case, 32 reflections with $20.0^\circ \leq 2\theta \leq 22.0^\circ$ were used to refine the cell parameters. Using the ω-scan method, 2271 reflections were collected. Four reflections were measured every 96 reflections to monitor instrument and crystal stability (Maximum correction on I was < 1%). Absorption corrections were applied based on measured crystal faces using *SHELXTL plus* ;[41] absorption coefficient, $\mu = 1.13$ mm^{-1} (min. and max. transmission factors are 0.840 and 0.958, respectively).

The structure was solved by direct methods in *SHELXTL plus* and refined using full-matrix least squares. The hexafluorophosphate ion is disordered and two partial ions were refined; the P atom is common to both of them. F1, F2 and F3 belong to one part and F1', F2' and F3' to the other. Their site-occupation-factors were changed repeatedly in every refinement until values of 0.60 and 0.40, respectively gave the best refinement results. The non-H atoms were treated anisotropically, whereas the positions of the hydrogen atoms were calculated in ideal positions and their isotropic thermal parameters were fixed. There are 159 parameters were refined and $\Sigma\omega(|F_o| - |F_c|^2$ was minimized; $\omega = 1/(\sigma|F_o|)^2$, $\sigma(F_0) = 0.5kI^{-1/2}\{|\sigma(I)|^2 + (0.02I)^2\}^{1/2}$, I(intensity)= ($I_{peak} - I_{background}$)(scan rate), and $\sigma(I) = (I_{peak} + I_{background})^{1/2}$ (scan rate), k is the correction due to decay and L_p effects, 0.02 is a factor used to down weight intense reflections and to account for instrument instability. The linear absorption coefficient was calculated from values from the *International Tables for X-ray Crystallography* .[42] Scattering factors for non-hydrogen atoms were taken from Cromer & Mann [43] with anomalous-dispersion corrections from Cromer & Liberman ,[44] while those of hydrogen atoms were from Stewart, Davidson & Simpson .[45]

173 K Data were collected at 173 K on a Siemens SMART PLATFORM diffractometer equipped with a CCD area detector and a graphite monochromator utilizing

MoK_α radiation (l = 0.71073 Å). 3273 reflections (1773 unique and 1723 > 2σ (F)) were collected from 1475 frames using the ω-scan method. Frame width was 0.3° and frame exposure time was 30 second. Absorption corrections were applied based on measured crystal faces using *SHELXL5*; absorption coefficient, $\mu = 1.158\ mm^{-1}$ (min. and max. transmission factors are 0.732 and 0.854, respectively).

The structure was solved by direct methods in *SHELXL5* and refined using full-matrix least squares. The non-H atoms were treated anisotropically, whereas the hydrogen atoms were refined with isotropic thermal parameters. The linear absorption coefficient, scattering factors for non-hydrogen atoms, and anomalous-dispersion corrections were taken from values from the *International Tables for X-ray Crystallography*.

Temperature-dependent ESR Experiment

Electron Spin Resonance spectra were recorded by use of a Bruker ER-200 spectrometer from 298 K to 4 K. A (BEDT-TTF)PF_6* single crystal was selected and mounted on a cut edge of a quartz rod (Figure 5-2) and rotation (Figure 5-3) was achieved using a home-built goniometer. Samples were cooled using an ESR 900 Cryostat. The temperature was measured with a AuFe/Ch thermocouple. The temperature-dependent electron spin resonance (ESR) data were obtained for a single crystal (1.25 X 1.0 X 0.06 mm) of (BEDT-TTF)PF_6* at 9.26 GHz with 100 KHz field modulation.

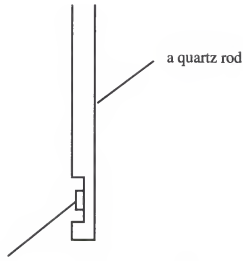

Figure 5-1. (BEDT-TTF)PF_6* was mounted on a cut edge of a quartz rod.

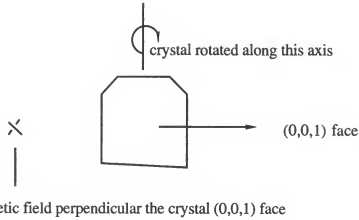

Figure 5-2. The rotation of (BEDT-TTF)PF_6* in ESR experiment.

Transport Measurements

The measurement was performed by Garret E. Granroth in department of physics. Needle-shaped crystals of (BEDT-TTF)PF_6* (typically 1.0 x 0.13 x 0.04 mm^3) were measured in this study. Temperature-dependent (294-180 K) ac resistances[2] were measured by the four-probe method. Narrow gauge (0.02 mm diameter) gold wires were affixed to the crystal under a microscope using fast drying gold paint. The sample was put

onto a chip which fits onto our homebuilt low temperature dipstick. A typical run was done by first cooling down the sample to low temperature, and taking the data while warming up. Temperature reproducibility obtained in this set-up has been determined to be ± 0.5 K or better over the temperature range measured.

Optical Measurements

The optical measurements were completed by Hsiang-Lin Liu in the Department of Physics. Near normal polarized reflectance measurements were made on single-crystal samples. Far-infrared (FIR) and mid-infrared (MIR) measurements were carried out on an IBM-Bruker 113V Fourier-transform infrared spectrometer from 30 to 4000 cm^{-1} with a bolometer detector (30-600 cm^{-1}) and a B-doped Si photoconductor (450-4000 cm^{-1}). Wire grid polarizers on polyethelene and AgBr were used in the FIR and MIR, respectively. A Perkin-Elmer 16U grating spectrometer was used to measure the spectra in the infrared to the ultraviolet (1000-32000 cm^{-1}), using wire grid and dichroic polarizers. For low-temperature measurements, the sample was mounted in a continuous-flow helium cryostat equipped with a thermometer and heater near the cryostat tip, regulated by a temperature controller.

Experiments were performed in two polarizations: with light polarized parallel and perpendicular to the BEDT-TTF chain axis. The reflectance was calibrated with a reference aluminum mirror. In order to compensate for the scattering losses, all samples were coated with a thin aluminum layer after the optical measurement was finished. The final corrected reflectance was obtained by evaluating the initial reflectance (no coating) to the reflectance of the coated sample, then multiplying the ratio by the aluminum reflectance from the literature.[79] After the reflectance spectra over a wide frequency were measured, the optical properties were determined by the Kramers-Kronig analysis.

Magnetic Measurements

Measurements on the (BEDT-TTF)PF_6* were completed by Dr. Mark W. Meisel in Department of Physics. The temperature dependence of the magnetic susceptibility was obtained from magnetization measurements made with a Quantum Design (San Diego, CA) Model MPMS magnetometer operating at 1 kG. A 5.9 mg sample of crystals was put in #5 gelatine capsule and pieces of plastic straw were used as the sample holder during the measurements. The magnetic signal arising from the plastic is well characterized and has been subtracted from the results.

Results

Synthesis and Structure

In the PF_6 family of BEDT-TTF salts, the oxidation state of BEDT-TTF is most often +1/2. Exceptions are (BEDT-TTF)PF_6*, δ-(BEDT-TTF)PF_6, and ε-(BEDT-TTF)PF_6 where oxidation state of BEDT-TTF is +1. During the synthesis of (BEDT-TTF)PF_6*, allowing air into the cell and using undistilled CH_2Cl_2 increased the selectivity of the (BEDT-TTF)PF_6* phase. Instead of obtaining (BEDT-TTF)PF_6* , we got the β-(BEDT-TTF)$_2PF_6$ when using distilled CH_2Cl_2 or puting Ar into the cell. The reason is probably that the traces of oxygen and moisture increase the oxidizing ability of the whole system. Under the right conditions, we obtain three kinds of crystals. (BEDT-TTF)PF_6* forms as very thin hexagonal plates, δ-(BEDT-TTF)PF_6 forms as small needle-like crystals and ε-(BEDT-TTF)PF_6 forms as small rock-like crystals. The structures of the three salts are different, (BEDT-TTF)PF_6* and δ-(BEDT-TTF)PF_6 crystalling in the triclinic space group $P\bar{1}$, and ε-(BEDT-TTF)PF_6 crystalling in the monoclinic C2/m.[83] The structures of δ and ε have been reported previously.[83] Crystallographic data for (BEDT-TTF)PF_6* are presented in Appendix Table C-1. Atomic coordinates are listed in Appendix Table C-2, and bond lengths and angles are presented in Appendix Table C-3. The 173 K data are

presented in Appendix Table C-7 through C-10. Figures 5-3, 5-4, and Figure 5-5 show packing diagrams for (BEDT-TTF)PF_6*, δ-(BEDT-TTF)PF_6, and ε-(BEDT-TTF)PF_6 [91] including both anions and cations. In (BEDT-TTF)PF_6*, intermolecular overlap between donor is weak and the nearest intermolecular S-S contact is 3.688 Å along the x direction. In the 173K structure, the nearest intermolecular S-S contact along the x direction is 3.590 Å. The distance of the BEDT-TTF central carbon-carbon bond is 1.398(6) Å at room temperature, and it is 1.382(4) Å at 173K. Although the central bond distance decreases in the 173 K structure, it is still in a reasonable range for 1:1 BEDT-TTF salts.[81] The main difference between the high and low temperature structures is that the PF_6^- anions are disordered at room temperature, but are ordered at 173K. In δ-(BEDT-TTF)PF_6, the donor molecules are strongly dimerized compared to (BEDT-TTF)PF_6*. The nearest intermolecular S-S contact is 3.607 Å in δ-(BEDT-TTF)PF_6. In ε-(BEDT-TTF)PF_6, all BEDT-TTF monocations are equivalent and are surrounded by six counterions in a distorted octahedron. There is no intermolecular overlap between donor molecules in ε-(BEDT-TTF)PF_6.

Optical Measurement

Figure 5-6 displays the room temperature reflectance of (BEDT-TTF)PF_6* over the entire spectral range for polarizations parallel and perpendicular to the BEDT-TTF stacking axis. The optical absorption coefficient, α (determined by Kramers-Kronig analysis of the reflectance)[94] is shown in Figure 5-7. Note the logarithmic wavelength scale. For the electric-field vector polarized along the BEDT-TTF chain direction, the spectrum shows several electronic excitations (at ~ 1550 nm and 700 ~ 400 nm). The low-energy band contains a majority of the oscillator strength. This electronic feature could be attributed to the transfer of charge between BEDT-TTF molecules within the stack. Other higher-energy bands are thought to be intramolecular localized excitations or molecular excitons. In contrast, the infrared spectrum is dominated by many sharp vibrational features polarized along the chain axis. Many of these modes are the total symmetric (A_g) vibrations of the

Figure 5-3. View of the 173 K crystal structure showing the molecular packing of (BEDT-TTF)PF_6*.

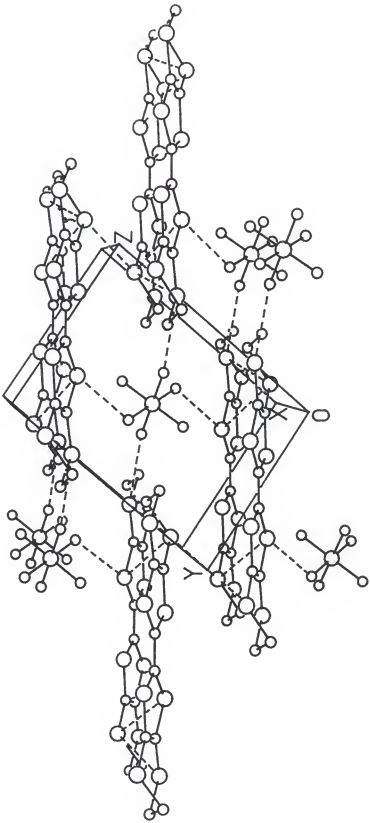

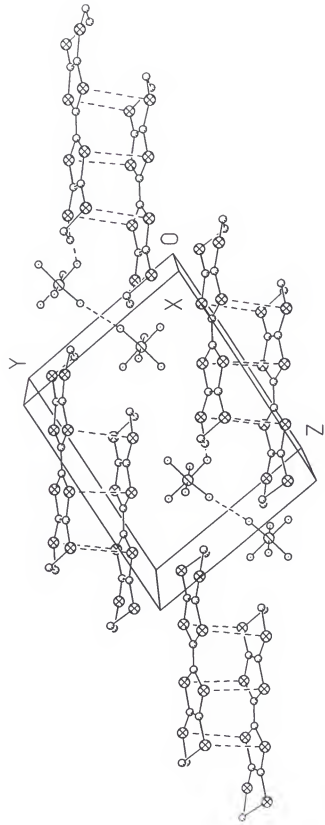
O
X
Y
Z

Figure 5-5. View showing the molecular packing of ε-(BEDT-TTF)PF_6.[91]

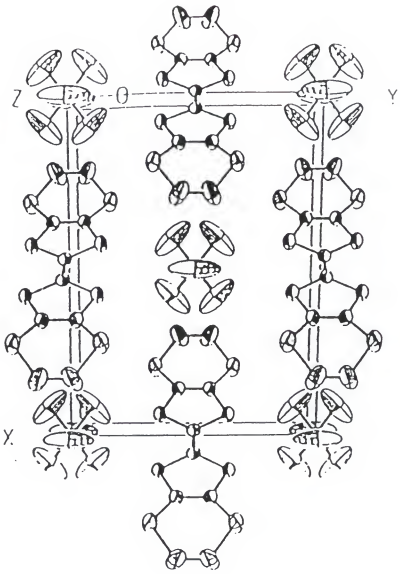
Z
O
Y
X

Figure 5-6. Optical reflectivity data from (BEDT-TTF)PF_6* polarized along the a and b axes.

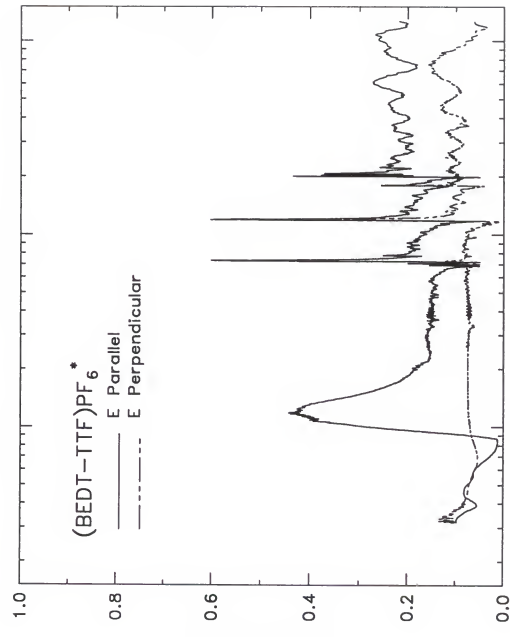
(BEDT-TTF)PF6*
E Parallel
E Perpendicular
Reflectance
1.0
0.8
0.6
0.4
0.2
0.0
0.01
0.1
1
Wavelength (nm) (10^5)

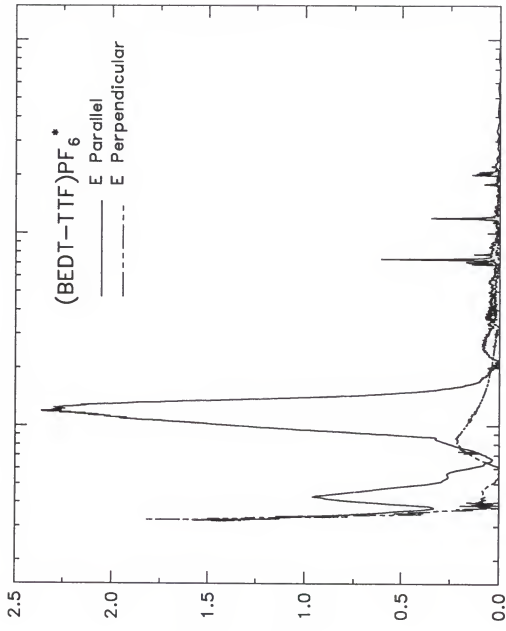
(BEDT–TTF)PF6*
E Parallel
E Perpendicular
α (cm⁻¹) (10⁵)
2.5
2.0
1.5
1.0
0.5
0.0
0.01
0.1
1
Wavelength (nm) (10⁵)

BEDT-TTF molecules, activated by coupling to charge transfer excitations.[95] Additional vibrational structure is much weaker and is due to BEDT-TTF modes of other symmetry as well as vibration due to the PF_6^- anions. Perpendicular to the BEDT-TTF stacking direction, the reflectivity is low (~ 10 %), flat, and almost featureless.

To compare the spectral differences as a function of temperature, the far-infrared reflectivity is shown in Figure 5-8 for three temperatures, 100, 200, and 300 K. The vibrational triplets (at ~ 20 μm) which are PF_6^- vibrational modes appear only at room temperature. Only a single line is seen at lower temperatures. From the 173K (BEDT-TTF)PF_6* structure data, there is a PF_6^- transition from disordered to ordered around 250K. This indicates that the PF_6^- molecules are frozen during the cooling; its structure becomes more uniform upon cooling from 300 K to 200 K. Upon further cooling, we observed no significant temperature variation between 100 K and 25 K.

Conductivity

Four-probe electrical conductivity measurements are shown in Figure 5-9. The (BEDT-TTF)PF_6* behaves as a semiconductor with a room temperature conductivity of 1.1 X 10^{-4} $\Omega^{-1}cm^{-1}$. The conductivity decreases from its 294 K value when the temperature is decreased. The temperature dependence of a semiconductor may be expressed as equation 5-1. The data from Figure 5-9 can be treated using equation 5-1 over the temperature range above 240 K yieldings an activation energy $E_a = E_g/2$ of 0.55 eV.

$$\sigma(T) = \sigma_o \exp(- E_g/2k_BT) \qquad (5\text{-}1)$$

Figure 5-8. Optical reflectivity data from (BEDT-TTF)PF_6* polarized along the b axis at 100, 200, and 300 K.

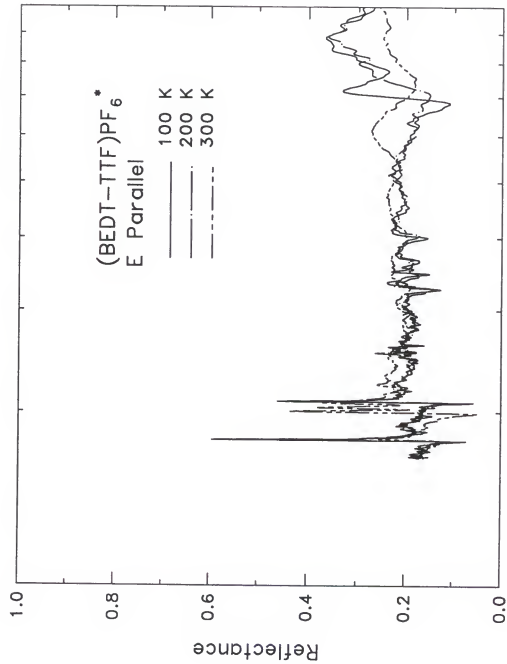
(BEDT-TTF)PF6
E Parallel
100 K
200 K
300 K
Reflectance
Wavelength (μm)
1.0
0.8
0.6
0.4
0.2
0.0
10
100

Figure 5-9. Electrical conductivity of (BEDT-TTF)PF6* from 298 to 200 K showing semiconductor behavior.

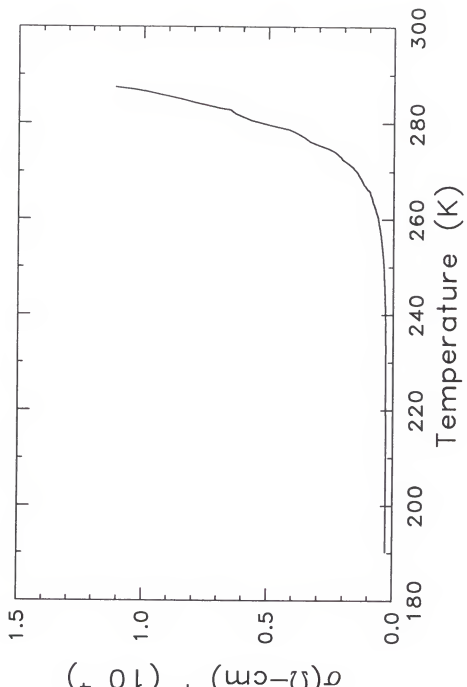
1.5
1.0
0.5
0.0
180
200
220
240
260
280
300
Temperature (K)
σ(Ω-cm)⁻¹ (10⁻⁴)

ESR Measurements

At room temperature, we can use the peak-to-peak first derivative Lorentzian ESR line widths (ΔH_{p-p}) to discern the different packing forms in the (BEDT-TTF)PF_6 family. (See Table 5-1)

crystal forms	peak-to-peak width (Gauss)
(BEDT-TTF)PF_6*	9.38
δ-(BEDT-TTF)PF_6	no signal
ε-(BEDT-TTF)PF_6	4.52
β-(BEDT-TTF)$_2PF_6$	21.82

Table 5-1. Peak-to-peak widths (ΔH_{p-p}) of (BEDT-TTF)PF_6 family at room temperature.

Figure 5-10 illustrates the spin susceptibility (in arbitrary units measured from the intergrated area of the ESR signal) and figure 5-11 shows the peak-to-peak derivative ESR linewidths (ΔH_{p-p}) that were measured from 298 K to 4 K with the static magnetic field approximately parallel to the crystallographic c axis (crystal plate normal). The value of ΔH_{p-p} was 9.38 Gauss at 298 K and decreased approximately linearly with temperature to 1.37 Gauss at 30.3 K, at which point there is no signal as the temperature was lowered further. The spin susceptibility dropped gradually with decreasing temperature from 298 to 230 K. This seems to be associated with the anion ordering transition. A second decrease occurs below 100 K until below about 30 K, there is no signal. The g-value for this ESR signal (calibrated with DPPH single crystal) was relatively constant between 298 to 30 K, with deviations of only ±0.002 from 2.010.

Figure 5-10. Temperature dependence of the integral area of the ESR signal showing the phase transition of (BEDT-TTF)PF_6* at around 30 K.

The susceptibility from 298 K to 4 K of (BEDT-TTF)PF6*

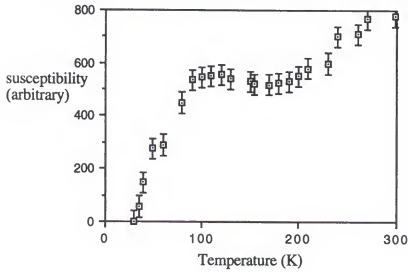

Figure 5-11. Temperature dependence of the peak-to-peak linewidths (Gauss) of the ESR signal at (BEDT-TTF)PF_6*. The single crystal was oriented with the c axis nearly parallel to the static magnetic field.

The Linewidth from 298 K to 4 K of (BEDT-TTF)PF6*

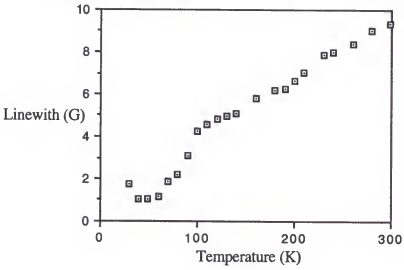

Magnetic Susceptibility Measurements

The temperature dependence of the molar susceptibility, χ, is plotted in figure 5-12. The data have been corrected for a diamagnetic core contribution calculated using Pascal's constants.[92] The correction is $1.4 \pm 0.4 \times 10^{-4}$ emu/mol. The maximum χ is 3.5×10^{-4}. The χ droped gradually with decreasing temperature from 298 to 230 K. This result is the same tendency seen with the ESR data. In the range 230 to 30 K, the χ decreases from 2.4×10^{-4} emu/mol to 1.4×10^{-4} emu/mol. From 30 to 4 K the χ drops sharply and a small Curie tail is present corresponding to s = 1/2 impurities.

Discussion

Structure

There are now several different BEDT-TTF monocation structures. In δ-(BEDT-TTF)PF_6 and (BEDT-TTF)$Ag_4(CN)_5$,[86] the BEDT-TTF packing styles are similar to the δ-(BEDT-TTF)$_2I_3$ [93] structure. However, in ε-(BEDT-TTF)PF_6, the BEDT-TTF molecules are well separated by PF_6^- anions and this structure is exactly the same as (BEDT-TTF)$AuBr_2Cl_2$.[87] In (BEDT-TTF)PF_6*, the close contacts of BEDT-TTF in the x direction are 3.688 Å at room temperature and 3.590 Å at 173 K. The interactions along the z direction BEDT-TTF stacking axis are small at both temperatures. The z direction distances between two BEDT-TTF are 3.75 Å at room temperature and 3.72 Å at 173 K in this direction. This distance is slightly larger than S-S van der Waals distance. In the y direction, the BEDT-TTF molecule is well separated by the PF_6^- molecule. From the structure of (BEDT-TTF)PF_6*, we can say it might have quasi-1D properties with the x axis the direction of largest interaction. There is a structural transition around 250K. This is due to ordering of the PF_6^- anions, but the whole packing style of the BEDT-TTF molecules are not changed. We can easily see the change in both the optical and x-ray data.

Figure 5-12. The temperature dependent magnetic susceptibility, χ, of (BEDT-TTF)PF_6*. The data have been corrected for a diamagnetic core contribution calculated using Pascal's constants.[92] The correction is $1.4 \pm 0.4 \times 10^{-4}$ emu/mol.

χ (emu/mol)
4x10⁻⁴
3x10⁻⁴
2x10⁻⁴
1x10⁻⁴
0
0
50
100
150
200
250
300
T (K)

Magnetic data

Qualitatively, a spin-Peierls[85] transition can be described as a magnetoelastic transition whereby a 1D antiferromagnetically coupled chain of localized spins couples with a 3D phonon, resulting in a lattice distortion to an alternating linear Heisenberg chain. In the BEDT-TTF family, α'-(BEDT-TTF)$_2$Ag(CN)$_2$ [85] is the only salt to show a transition due to the spin-Peierls mechanism. The maximun χ is 2 x 10^{-3} emu/mole and nearest neighbour exchange (J/k_B) is 56K. The maximum χ is 3.5 x 10^{-4} emu/mole in (BEDT-TTF)PF_6*, this value is smaller than α'-(BEDT-TTF)$_2$Ag(CN)$_2$. [85] Possible reasons for the small susceptibility are that (BEDT-TTF)PF_6* might have a very large J/k_B value or it has a higher dimensional structure. For (BEDT-TTF)PF_6*, as the temperature is decreased below 30 K, the ESR spectrum disappears and the magnetic susceptibility data χ drops sharply toward zero (considering the uncertainty in measurement). This behavior is consistent with a spin-Peierls transition.[85] Since the spin-peierls transition is a second-order transition and the ground state is not magnetic, the structural dimerization may occur before the magnetic transition.

Conclusions

We report the structure, ESR, magnetic susceptibility, optical, and transport data of (BEDT-TTF)PF_6*. There is a structural transiton around 250 K associated with PF_6^- ordering. At 30 K, (BEDT-TTF)PF_6* has a magnetic transition which is an insulator to insulator transition. The magnetic data for (BEDT-TTF)PF_6* are consistent with a spin-Peierls transition at 30 K. In the BEDT-TTF family, this is the first example 1:1 salt which has the spin-Peierls transition.

APPENDIX
TABLES OF CRYSTALLOGRAPHIC DATA

Appendix Table A-1: Crystallographic data for TMNIN.

A. Crystal data (293 K)	**I**
a, Å	9.1029(9)
b, Å	9.1029(9)
c, Å	7.0816(7)
α, deg.	90
β, deg.	90
γ, deg.	120
V, Å^3	508.18(8)
d_{calc}, g cm^{-3}(293 K)	1.770
Empirical formula	$[(CH_3)_4N][Ni(NO_2)_3]$
Formula wt, g	270.89
Crystal system	Trigonal
Space group	$P\bar{3}m1$
Z	2
F(000), electrons	280
Crystal size (mm^3)	0.30 x 0.04 x 0.04
B. Data collection (293 K)	
Radiation, l (Å)	Mo-K_α, 0.71073
Mode	w-scan
Scan rang	Symmetrically over 1.2∞ about $K_{\alpha 1,2}$ maximum
Background	offset 1.0 and -1.0 in w from $K_{\alpha 1,2}$ maximum
Scan rate, deg. min.$^{-1}$	2 – 4
2q range, deg.	3 – 55
Range of *h k l*	$0 \leq h \leq 11$ $-11 \leq k \leq 11$ $-9 \leq l \leq 9$
Total reflections measured	2497
Unique reflections	472
Absorption coeff. m (Mo-K_α), mm^{-1}	1.93
C. Structure refinement	
S, Goodness-of-fit	0.97
Reflections used, I > 2σ(I)	359
No. of variables	45
R, wR* (%)	2.50, 2.82
R, wR* , all data (%)	4.20, 3.68
R_{int}. (%)	2.70
Max. shift/esd	0.001

Appendix Table A-1 continued.

min. peak in diff. four. map (e $Å^{-3}$)	-0.33
max. peak in diff. four. map (e $Å^{-3}$)	0.33

* Relevant expressions are as follows, where in the footnote F_o and F_c represent, respectively, the observed and calculated structure-factor amplitudes.

Function minimized was $w(|F_o| - |F_c|)^2$, where $w = (\sigma(F))^{-2}$

$R = \Sigma(||F_o| - |F_c||) / \Sigma|F_o|$

$wR = [\Sigma w(|F_o| - |F_c|)^2 / \Sigma |F_o|^2]^{1/2}$

$S = [\Sigma w(|F_o| - |F_c|)^2 / (m-n)]^{1/2}$

Appendix Table A-2: Fractional coordinates and equivalent isotropic[a] thermal parameters ($Å^2$) for the non-H atoms of compound **TMNIN**.

Atom	x	y	z	U
Ni1	0.0	0.0	0.0	0.0238(2)
Ni2	0.0	0.0	0.5	0.0254(3)
N1	0.2192(3)	0.1096(2)	0.1661(3)	0.024(1)
O1	0.2193(3)	0.1097(1)	0.3468(3)	0.031(1)
O2	0.3585(3)	0.1793(1)	0.0923(3)	0.043(1)
N2	0.3333	0.6667	0.3492(6)	0.027(1)
C1	0.3333	0.6667	0.5604(8)	0.041(2)
C2	0.4225(3)	0.8451(5)	0.2808(7)	0.044(2)

[a]For anisotropic atoms, the U value is U_{eq}, calculated as $U_{eq} = 1/3 \sum_i \sum_j U_{ij} a_i^* a_j^* A_{ij}$ where A_{ij} is the dot product of the i^{th} and j^{th} direct space unit cell vectors.

Appendix Table A-3: Selected Bond Lengths (Å) and Angles (°) for the non-H atoms of compound
TMNIN

1	2	3	1-2	1-2-3
N1	Ni1	N1a	2.090(2)	180.00(0)
N1	Ni1	N1b		91.44(8)
N1	Ni1	N1c		88.56(8)
N1	Ni1	N1d		91.44(6)
N1	Ni1	N1e		88.56(6)
O1	Ni2	O1a	2.041(2)	180.00(0)
O1	Ni2	O1b		85.62(5)
O1	Ni2	O1c		94.38(5)
O1	Ni2	O1d		85.62(7)
O1	Ni2	O1e		94.38(7)
O1	N1	O2	1.280(3)	115.4(2)
O1	N1	Ni1		124.3(2)
O2	N1	Ni1	1.218(3)	120.3(2)
Ni2	O1	N1		122.1(2)
C1	N2	C2	1.495(7)	109.0(2)
C1	N2	C2a		109.0(2)
C2	N2	C2a	1.487(4)	109.9(3)
C2	N2	C2b		109.9(3)
C2a	N2	C2b	1.487(4)	109.9(3)
C2b	N2	C1	1.487(4)	109.0(2)

N1x and O1x, where x= a,b,c,d,e, are derived from N1 and O1, respectively, using the $\bar{3}$ symmetry operator. C2a and C2b are derived from C2 by applying the 3-fold rotation symmetry at 1/3, 2/3, z.

Appendix Table B-1: Crystallographic data for BEDT-TTF$(BF_4)_2$ (1) and BEDT-TTF$(ClO_4)_2$ (2)

A. Crystal data (298 K)	**1**	**2**
a, Å	5.824(1)	5.867(1)
b, Å	9.490(2)	9.579(2)
c, Å	17.593(3)	17.669(3)
β, deg.	91.61(1)	92.06(2)
V, Å^3	972.0(3)	992.4(3)
d_{calc}, g cm^{-3}(298 K)	1.908	1.953
Empirical formula	$C_{10}H_8S_8^{2+}(BF_4^{1-})_2$	$C_{10}H_8S_8^{2+}(ClO_4^{1-})_2$
Formula wt, g	279.13	291.77
Crystal system	Monoclinic	Monoclinic
Space group	$P2_1/n$	$P2_1/n$
Z	2	2
Crystal size (mm^3)	0.34 x 0.13 x 0.08	0.28 x 0.22 x 0.02
B. Data collection (298 K)		
Radiation, l (Å)	Mo-K_α, 0.71073	
Mode	w-scan	
Scan range	Symmetrically over 1.2∞ about $K_{\alpha 1,2}$ maximum	
Background	offset 1.0 and -1.0 in w from $K_{\alpha 1,2}$ maximum	
Scan rate, deg. min.$^{-1}$	2 – 4	2 - 4
2q range, deg.	3 – 50	3 – 50
Range of *h k l*	$0 \le h \le 6$; $-11 \le k \le 11$; $-20 \le l \le 20$	$0 \le h \le 6$; $0 \le k \le 11$; $-21 \le l \le 21$
Total reflections measured	3800 (2 sets)	2053
Unique reflections	1710	1742
Absorption coeff. m (Mo-K_α), mm^{-1}	0.99	1.21
Min. & Max. Transmission	0.885 & 0.936	0.787 & 0.982
C. Structure refinement		
S, Goodness-of-fit	1.43	1.44
Reflections used	1441, I > 2σ(I)	1385, I > 2σ(I)
No. of variables	146	162
R, wR* (%)	4.30, 4.33	3.31, 4.07
$R_{int.}$ (%)	0.0187	0.0113
Max. shift/esd	0.001	0.001

Appendix Table B-1 continued.

min. peak in diff. four. map (e $Å^{-3}$)	-0.20	-0.26
max. peak in diff. four. map (e $Å^{-3}$)	0.31	0.34

* Relevant expressions are as follows, where in the footnote F_o and F_c represent, respectively, the observed and calculated structure-factor amplitudes.

Function minimized was $w(|F_o| - |F_c|)^2$, where $w = (\sigma(F))^{-2}$

$R = \Sigma(||F_o| - |F_c||) / \Sigma|F_o|$

$wR = [\Sigma w(|F_o| - |F_c|)^2 / \Sigma |F_o|^2]^{1/2}$

$S = [\Sigma w(|F_o| - |F_c|)^2 / (m-n)]^{1/2}$

Appendix Table B-2: Fractional coordinates and equivalent isotropic[a] thermal parameters ($Å^2$) for the non-H atoms of compound 1 and 2

Atom	x	y	z	U
Compound 1				
S1	0.10314(13)	0.21502(8)	0.02273(5)	0.0413(2)
S2	-0.26559(13)	0.05037(7)	0.07803(4)	0.0405(2)
S3	-0.0049(2)	0.47397(8)	0.10514(5)	0.0521(3)
S4	-0.46598(14)	0.27055(8)	0.17201(5)	0.0469(3)
C1	-0.0351(5)	0.0586(3)	0.0225(2)	0.0320(8)
C2	-0.0745(5)	0.2997(3)	0.0840(2)	0.0351(9)
C3	-0.2524(5)	0.2210(3)	0.1105(2)	0.0342(9)
C4	-0.2645(13)	0.5321(6)	0.1461(6)	0.045(2)
C4'	-0.182(3)	0.5025(13)	0.1856(9)	0.046(4)
C5	-0.352(2)	0.4364(9)	0.2072(5)	0.041(2)
C5'	-0.431(3)	0.4604(13)	0.1764(13)	0.051(4)
B	0.2002(6)	0.3236(4)	0.3501(2)	0.0403(11)
F1	0.1799(4)	0.4685(2)	0.34556(13)	0.0715(7)
F2	0.0988(4)	0.2779(2)	0.41713(12)	0.0661(8)
F3	0.0981(4)	0.2607(3)	0.28799(13)	0.0757(9)
F4	0.4320(3)	0.2911(2)	0.35371(12)	0.0655(7)
Compound 2				
S1	0.1024(2)	0.21253(8)	0.02324(5)	0.0412(3)
S2	-0.2630(2)	0.04883(8)	0.07734(5)	0.0404(3)
S3	-0.0058(2)	0.46836(9)	0.10523(6)	0.0533(3)
S4	-0.4619(2)	0.26610(9)	0.17077(6)	0.0468(3)
C1	-0.0355(6)	0.0579(3)	0.0227(2)	0.0326(10)
C2	-0.0742(6)	0.2964(3)	0.0840(2)	0.0366(11)
C3	-0.2515(6)	0.2173(3)	0.1100(2)	0.0323(10)
C4	-0.265(2)	0.5254(8)	0.1438(9)	0.049(3)
C4'	-0.187(3)	0.498(2)	0.1844(12)	0.039(4)
C5	-0.353(2)	0.4336(10)	0.2050(8)	0.043(3)
C5'	-0.432(4)	0.453(2)	0.172(2)	0.044(5)
Cl	0.1979(2)	0.31952(8)	0.34856(5)	0.0403(3)
O1	0.1731(5)	0.4678(3)	0.3410(2)	0.0649(11)
O2	0.0939(5)	0.2740(3)	0.4169(2)	0.0614(11)
O3	0.0945(5)	0.2514(3)	0.2847(2)	0.0685(12)
O4	0.4361(5)	0.2876(3)	0.3528(2)	0.0584(10)

[a]For anisotropic atoms, the U value is U_{eq}, calculated as $U_{eq} = 1/3 \sum_i \sum_j U_{ij} a_i^* a_j^* A_{ij}$ where A_{ij} is the dot product of the i^{th} and j^{th} direct space unit cell vectors.

Appendix Table B-3: Bond Lengths (Å) and Angles (°) for the non-H atoms of compound 1 and 2

1	2	3	1-2	1-2-3
Compound 1				
C1	S1	C2	1.689(3)	96.77(14)
C2	S1		1.715(3)	
C1	S2	C3	1.684(3)	96.91(14)
C3	S2		1.718(3)	
C2	S3	C4	1.740(3)	100.7(2)
C4	S3		1.781(9)	
C2	S3	C4'		100.1(4)
C4'	S3		1.80(2)	
C3	S4	C5	1.737(3)	100.8(3)
C5	S4		1.810(9)	
C3	S4	C5'		102.3(6)
C5'	S4		1.814(13)	
C1a	C1	S1	1.430(4)	122.8(2)
C1a	C1	S2		122.0(2)
S1	C1	S2		115.2(2)
C3	C2	S1	1.369(4)	115.7(2)
C3	C2	S3		128.3(2)
S1	C2	S3		116.0(2)
S2	C3	S4		115.9(2)
S2	C3	C2		115.4(2)
S4	C3	C2		128.8(2)
C5	C4	S3	1.507(13)	114.2(5)
S4	C5	C4		114.0(6)
C5'	C4'	S3	1.51(2)	116.5(13)
S4	C5'	C4'		112.1(10)
F1	B	F3	1.382(4)	110.8(3)
F1	B	F4		107.9(3)
F2	B	F1	1.403(4)	108.6(3)
F2	B	F3		110.7(3)
F3	B	F4	1.366(4)	110.0(3)
F4	B	F2	1.385(4)	109.0(3)
Compound 2				
C1	S1	C2	1.688(3)	96.6(2)
C2	S1		1.717(3)	
C1	S2	C3	1.678(3)	97.0(2)
C3	S2		1.714(3)	
C2	S3	C4	1.734(3)	100.4(3)
C4	S3		1.774(12)	
C4'	S3	C2	1.81(2)	100.3(5)
C3	S4	C5	1.729(3)	101.3(5)
C5	S4		1.821(11)	
C5'	S4	C3	1.80(2)	101.7(9)

Appendix Table B-3 continued.

C1a	C1	S1	1.439(4)	122.1(2)
C1a	C1	S2		122.2(2)
S1	C1	S2		115.7(2)
C3	C2	S1	1.379(5)	115.5(2)
C3	C2	S3		128.4(3)
S1	C2	S3		116.1(2)
S2	C3	S4		116.3(2)
S2	C3	C2		115.2(2)
S4	C3	C2		128.5(2)
C5	C4	S3	1.50(2)	114.8(7)
C5'	C4'	S3	1.51(3)	115.(2)
S4	C5	C4		113.8(9)
S4	C5'	C4'		111.9(13)
O1	Cl	O2	1.434(3)	109.5(2)
O1	Cl	O3		110.0(2)
O2	Cl	O3	1.440(3)	110.2(2)
O2	Cl	O4		109.5(2)
O3	Cl	O4	1.421(3)	109.4(2)
O4	Cl	O1	1.430(3)	108.2(2)

Appendix Table B-4: Anisotropic thermal parameters[a] for the non-H atoms of compound 1

Atom	U11	U22	U33	U12	U13	U23
S1	0.0442(4)	0.0288(4)	0.0519(4)	-0.0078(3)	0.0218(3)	-0.0107(5)
S2	0.0469(4)	0.0258(4)	0.0501(4)	-0.0058(3)	0.0228(3)	-0.0070(5)
S3	0.0605(5)	0.0293(5)	0.0681(4)	-0.0118(4)	0.0285(4)	-0.0155(6)
S4	0.0493(5)	0.0371(5)	0.0556(4)	-0.0053(4)	0.0262(4)	-0.0146(5)
C1	0.0357(14)	0.0271(14)	0.0336(13)	-0.0004(12)	0.0076(11)	-0.0025(15)
C2	0.041(2)	0.027(2)	0.0387(14)	-0.0023(13)	0.0116(12)	-0.005(2)
C3	0.040(2)	0.027(2)	0.0365(14)	0.0025(12)	0.0075(12)	-0.004(2)
C4	0.047(4)	0.028(4)	0.060(3)	0.005(3)	0.012(3)	-0.004(5)
C4'	0.064(8)	0.037(8)	0.036(5)	0.004(6)	0.005(5)	-0.011(7)
C5	0.046(4)	0.032(4)	0.045(4)	0.003(3)	0.017(3)	-0.010(4)
C5'	0.054(8)	0.025(8)	0.074(5)	0.018(7)	0.010(6)	0.003(11)
B	0.042(2)	0.031(2)	0.048(2)	0.001(2)	0.009(2)	-0.000(2)
F1	0.0713(14)	0.0361(14)	0.1086(11)	0.0082(13)	0.0288(11)	0.006(2)
F2	0.0738(14)	0.0658(14)	0.0601(14)	-0.0049(11)	0.0240(10)	0.0017(13)
F3	0.088(2)	0.076(2)	0.063(2)	-0.0167(12)	-0.0043(12)	-0.0041(14)
F4	0.0556(12)	0.0714(12)	0.0701(14)	0.0229(10)	0.0139(11)	-0.0015(14)

[a] Uij are the mean-square amplitudes of vibration in $Å^2$ from the general temperature factor expression

$$\exp[-2\pi^2(h^2a^{*2}U11 + k^2b^{*2}U22 + l^2c^{*2}U33 + 2hka^*b^*U12 + 2hla^*c^*U13 + 2klb^*c^*U23)]$$

Appendix Table B-5: Fractional coordinates and isotropic thermal parameters ($Å^2$) for the H atoms of compound 1

Atom	x	y	z	U
H4a	-0.3816	0.5348	0.1066	0.08
H4b	-0.2453	0.6256	0.1660	0.08
H4'a	-0.1851	0.6028	0.1924	0.08
H4'b	-0.1058	0.4644	0.2301	0.08
H5a	-0.2210	0.4151	0.2395	0.08
H5b	-0.4633	0.4832	0.2376	0.08
H5'a	-0.4902	0.4865	0.2247	0.08
H5'b	-0.5186	0.5096	0.1378	0.08

Appendix Table B-6: Bond Lengths (Å) and Angles (°) of the H atoms of compound 1

1	2	3	1-2	1-2-3
H4a	C4	H4b	0.96(1)	107.8(9)
H4a	C4	S4		107.3(6)
H4a	C4	C5		105.6(8)
H4b	C4	S4	0.96(1)	110.3(7)
H4b	C4	C5		111.4(8)
H4'a	C4'	H4'b	0.96(2)	108.(2)
H4'a	C4'	S4		104.5(12)
H4'a	C4'	C5'		102.(2)
H4'b	C4'	S4	0.96(2)	113.3(14)
H4'b	C4'	C5'		116.(2)
H5a	C5	H5b	0.96(1)	108.2(7)
H5a	C5	C4		106.5(7)
H5a	C5	S3		108.0(8)
H5b	C5	C4	0.96(1)	109.6(10)
H5b	C5	S3		110.0(6)
H5'a	C5'	H5'b	0.96(1)	106.3(15)
H5'a	C5'	C4'		104.9(14)
H5'a	C5'	S3		105.1(12)
H5'b	C5'	C4'	0.96(2)	114.(2)
H5'b	C5'	S3		108.8(12)

Appendix Table C-1: Crystallographic data of $(BEDT\text{-}TTF)PF_6$*

A. Crystal data (298 K)

a, Å	6.274(1)
b, Å	7.360(1)
c, Å	9.888(1)
α, deg.	92.52(1)
β, deg.	93.27(1)
γ, deg.	98.77(1)
V, $Å^3$	449.9(1)
d_{calc}, g cm^{-3}(298 K)	1.955
Empirical formula	$C_{10}H_8S_8\ PF_6$
Formula wt, g	529.61
Crystal system	Triclinic
Space group	$P\bar{1}$
Z	1
F(000), electrons	265
Crystal size (mm^3)	0.25 x 0.15 x 0.04

B. Data collection (298 K)

Radiation, l (Å)	Mo-K_α, 0.71073
Mode	w-scan
Scan range	Symmetrically over 1.2∞ about $K_{\alpha 1,2}$ maximum
Background	offset 1.0 and -1.0 in w from $K_{\alpha 1,2}$ maximum

Appendix Table C-1 continued.

Scan rate, deg. min.$^{-1}$	3 – 6
2q range, deg.	3 – 55
Range of *h k l*	$0 \leq h \leq 8$
	$-9 \leq k \leq 9$
	$-12 \leq l \leq 12$

Total reflections measured	2271
Unique reflections	2081
Absorption coeff. m (Mo-K_α), mm^{-1}	1.13
Min. & Max. Transmission	0.840, 0.958

C. Structure refinement

S, Goodness-of-fit	1.45
Reflections used, $I > 2\sigma(I)$	1497
No. of variables	159
R, wR* (%)	4.96, 5.05
$R_{int.}$ (%)	1.55
Max. shift/esd	0.001
min. peak in diff. four. map (e Å^{-3})	-0.40
max. peak in diff. four. map (e Å^{-3})	0.39

* Relevant expressions are as follows, where in the footnote F_o and F_c represent, respectively, the observed and calculated structure-factor amplitudes.

Function minimized was $w(|F_o| - |F_c|)^2$, where $w = (\sigma(F))^{-2}$

$R = \Sigma(||F_o| - |F_c||) / \Sigma |F_o|$

$wR = [\Sigma w(|F_o| - |F_c|)^2 / \Sigma |F_o|^2]^{1/2}$

Appendix Table C-1 continued.

$S = [\Sigma w(|F_o| - |F_c|)^2 / (m-n)]^{1/2}$

Appendix Table C-2: Fractional coordinates and equivalent isotropic[a] thermal parameters ($Å^2$) for the non-H atoms of compound (BEDT-TTF)PF_6*. (I)

Atom	x	y	z	U
S1	0.3540(2)	0.83614(14)	0.65769(11)	0.0401(4)
S2	0.7454(2)	0.8220(2)	0.51684(11)	0.0410(4)
S3	0.3734(2)	0.5013(2)	0.80537(12)	0.0463(4)
S4	0.8542(2)	0.4915(2)	0.64702(12)	0.0474(4)
C1	0.5227(7)	0.9263(5)	0.5377(4)	0.0348(13)
C2	0.4913(6)	0.6530(5)	0.6910(4)	0.0325(12)
C3	0.6750(6)	0.6479(5)	0.6263(4)	0.0329(13)
C4	0.5652(7)	0.3438(6)	0.8269(5)	0.041(2)
C5	0.7967(7)	0.4278(7)	0.8164(5)	0.042(2)
P	0.0	0.0	0.0	0.0389(5)
F1	0.148(3)	-0.132(2)	-0.052(2)	0.116(6)
F2	0.163(2)	0.171(2)	-0.0348(12)	0.097(5)
F3	0.106(2)	0.006(2)	0.1474(10)	0.108(6)
F1'	0.104(4)	-0.175(3)	-0.051(2)	0.075(6)
F2'	0.111(3)	0.121(2)	-0.109(2)	0.110(9)
F3'	0.206(3)	0.044(3)	0.094(2)	0.143(9)

[a]For anisotropic atoms, the U value is U_{eq}, calculated as $U_{eq} = 1/3\ \Sigma_i\Sigma_j\ U_{ij}\ a_i^*\ a_j^*\ A_{ij}$ where A_{ij} is the dot product of the i^{th} and j^{th} direct space unit cell vectors.

Appendix Table C-3: Bond Lengths (Å) and Angles (°) for the non-H atoms of compound **I**.

1	2	3	1-2	1-2-3
C1	S1	C2	1.723(4)	95.4(2)
C2	S1		1.740(4)	
C1	S2	C3	1.712(4)	95.7(2)
C3	S2		1.736(4)	
C2	S3		1.740(4)	
C3	S4		1.738(4)	
S1	C1	S2		115.5(2)
C1a	C1	S1	1.398(6)	121.5(3)
C1a	C1	S2		122.9(3)
C3	C2	S1	1.354(6)	116.4(3)
C3	C2	S3		128.7(3)
S1	C2	S3		114.9(2)
S2	C3	S4		116.5(2)
S2	C3	C2		116.6(3)
S4	C3	C2		126.8(3)
C5	C4		1.500(6)	
F1	P	F2	1.54(2)	91.5(7)
F1	P	F3		92.0(8)
F1	P	F1a		180.(0)
F1	P	F2a		88.5(7)
F2	P	F3	1.558(11)	91.2(6)
F2	P	F1a		88.5(7)
F2	P	F2a		180.(0)

Appendix Table C-3 continued

F2	P	F3a		88.8(6)
F3	P	F1a	1.563(10)	88.0(8)
F3	P	F2a		88.8(6)
F3	P	F3a		180.(0)
F1a	P	F2a	1.54(2)	91.5(7)
F1a	P	F3a		92.0(8)
F2a	P	F3a	1.558(11)	91.2(6)
F3a	P	F1	1.563(10)	88.0(8)
F1'	P	F2'	1.61(2)	91.7(10)
F1'	P	F3'		84.3(11)
F1'	P	F1'a		180.(0)
F1'	P	F2'a		88.3(10)
F2'	P	F3'	1.56(2)	90.1(10)
F2'	P	F1'a		88.3(10)
F2'	P	F2'a		180.(0)
F2'	P	F3'a		89.9(10)
F3'	P	F1'a	1.53(2)	95.7(11)
F3'	P	F2'a		89.9(10)
F3'	P	F3'a		180.(0)
F1'a	P	F2'a	1.61(2)	91.7(10)
F1'a	P	F3'a		84.3(11)

Appendix Table C-3 continued.

F2'a	P	F3'a	1.56(2)	90.1(10)
F3'a	P	F1'	1.53(2)	95.7(11)

C1a from C1 by a center of inversion at (1/2 1 1/2).

F1a, F2a, F3a, F1'a, F2'a & F3'a obtained from F1, F2, F3, F1', F2' & F3', respectively, by a center of inversion at (0 0 0).

Appendix Table C-4: Anisotropic thermal parameters[a] for the non-H atoms of compound **I.**

Atom	U11	U22	U33	U12	U13	U23
S1	0.0451(6)	0.0347(5)	0.0451(6)	0.0164(5)	0.0081(5)	0.0105(5)
S2	0.0441(6)	0.0400(6)	0.0445(7)	0.0204(5)	0.0087(5)	0.0076(5)
S3	0.0416(6)	0.0475(7)	0.0597(8)	0.0312(6)	0.0154(5)	0.0132(5)
S4	0.0523(7)	0.0501(7)	0.0474(7)	0.0216(5)	0.0160(5)	0.0233(5)
C1	0.043(2)	0.023(2)	0.039(2)	0.009(2)	0.000(2)	-0.001(2)
C2	0.036(2)	0.028(2)	0.036(2)	0.012(2)	0.000(2)	0.003(2)
C3	0.040(2)	0.026(2)	0.034(2)	0.011(2)	0.002(2)	0.005(2)
C4	0.045(3)	0.034(2)	0.046(3)	0.015(2)	0.002(2)	0.006(2)
C5	0.042(3)	0.045(3)	0.042(3)	0.018(2)	-0.001(2)	0.009(2)
P	0.0429(9)	0.0280(8)	0.0490(10)	0.0131(7)	0.0072(7)	0.0069(7)
F1	0.144(10)	0.086(10)	0.147(10)	0.056(7)	0.095(8)	0.083(9)
F2	0.074(5)	0.065(5)	0.163(11)	0.044(7)	0.024(7)	-0.024(4)
F3	0.178(15)	0.087(6)	0.054(4)	0.004(4)	-0.030(6)	0.053(8)
F1'	0.137(13)	0.036(6)	0.053(7)	0.005(5)	0.005(8)	0.029(6)
F2'	0.14(2)	0.089(13)	0.138(14)	0.086(11)	0.093(13)	0.075(13)
F3'	0.085(11)	0.16(2)	0.15(2)	-0.054(15)	-0.077(11)	0.027(10)

[a] Uij are the mean-square amplitudes of vibration in $Å^2$ from the general temperature factor expression

$$\exp[-2\pi^2(h^2a^{*2}U11 + k^2b^{*2}U22 + l^2c^{*2}U33 + 2hka^*b^*U12 + 2hla^*c^*U13 + 2klb^*c^*U23)]$$

Appendix Table C-5: Fractional coordinates and isotropic thermal parameters ($Å^2$) for the H atoms of compound **I**.

Atom	x	y	z	U
H4a	0.518(7)	0.247(6)	0.759(5)	0.052(14)
H4b	0.539(8)	0.308(7)	0.918(5)	0.07(2)
H5a	0.827(6)	0.535(6)	0.877(4)	0.038(12)
H5b	0.898(7)	0.345(6)	0.844(4)	0.050(13)

Appendix Table C-6: Bond Lengths (Å) and Angles (°) of the H atoms of compound **I**.

1	2	3	1-2	1-2-3
H4a	C4	H4b	.96(4)	113.(4)
H4a	C4	C5		112.(3)
H4a	C4	S3		104.(3)
H4b	C4	C5	.97(5)	111.(3)
H4b	C4	S3		100.(3)
H5a	C5	H5b	.96(4)	107.(3)
H5a	C5	S4		109.(2)
H5a	C5	C4		108.(2)
H5b	C5	S4	.98(5)	107.(2)
H5b	C5	C4		113.(2)

Appendix Table C-7: Crystallographic data of (BEDT-TTF)PF_6* at 173K

A. Crystal data (173 K)	**I**
a, Å	6.2293(1)
b, Å	7.2633(2)
c, Å	9.8662(2)
α, deg.	93.898(1)
β, deg.	93.592(1)
γ, deg.	97.914(1)
V, $Å^3$	439.95(2)
d_{calc}, g cm^{-3}(173 K)	1.999
Empirical formula	$C_{10}H_8S_8PF_6$
Formula wt, g	529.61
Crystal system	Triclinic
Space group	P 1bar
Z	1
F(000), electrons	265
Crystal size (mm^3)	0.32 x 0.21 x 0.14
B. Data collection (173 K)	
Diffractometer	Siemens SMART PLATFORM
Detector	CCD area detector
Radiation, λ (Å)	Mo-K_α, 0.71073
Mode	ω-scan
Number of frames	1475
Frame width	0.3 deg.
Frame time	30 sec.
2q range, deg.	3 – 55
Range of *h k l*	-7 ≤ *h* ≤ 7 -9 ≤ *k* ≤ 9 -12 ≤ *l* ≤ 12
Total reflections measured	3273
Unique reflections	1773
Absorption coeff. m (Mo-K_α), cm^{-1}	1.158
Min. & Max. Transmission	0.732, 0.854
C. Structure refinement	
S, Goodness-of-fit	1.11
No. of variables	131
R (%) [$I > 2\sigma(I)$]	3.27, 1723
wR_2 (%) all reflections	7.82, 1723
$R_{int.}$ (%)	
Max. shift/esd	0.001

Appendix Table C-7 continued.

min. peak in diff. four. map (e $Å^{-3}$)	-0.61
max. peak in diff. four. map (e $Å^{-3}$)	0.51

* Relevant expressions are as follows, where in the footnote F_o and F_c represent, respectively, the observed and calculated structure-factor amplitudes.

Function minimized was $\omega(|F_o| - |F_c|)^2$, where$w = [1/[\sigma^2(F^2)+(0.0286P)^2 + 0.4320P]$,

where $P = (F_o^2 + 2F_c^2)/3$

R_1 Refinement on Structure factors

wR_2 Refinement on Structure factors squared.

Appendix Table C-8: Fractional coordinates and equivalent isotropic[a] thermal parameters ($Å^2$) for the non-H atoms of compound (BEDT-TTF)PF_6*

Atom	x	y	z	U
S(1)	0.1424(1)	0.6620(1)	0.8421(1)	0.021(1)
S(2)	-0.2503(1)	0.6808(1)	0.9847(1)	0.021(1)
S(3)	0.1121(1)	0.9944(1)	0.6915(1)	0.023(1)
S(4)	-0.3730(1)	1.0068(1)	0.8511(1)	0.024(1)
C(1)	-0.0230(3)	0.5734(3)	0.9632(2)	0.019(1)
C(2)	-0.0009(3)	0.8456(3)	0.8080(2)	0.018(1)
C(3)	-0.1850(3)	0.8527(3)	0.8735(2)	0.018(1)
C(4)	-0.0828(3)	0.11577(3)	0.6750(2)	0.021(1)
C(5)	-0.3153(3)	0.10684(3)	0.6812(2)	0.021(1)
P	0.5000	0.5000	0.5000	0.019(1)
F(1)	0.3650(3)	0.6559(2)	0.5579(2)	0.039(1)
F(2)	0.3274(3)	0.3389(2)	0.5477(2)	0.048(1)
F(3)	0.3660(3)	0.4908(2)	0.3562(2)	0.050(1)

[a]For anisotropic atoms, the U value is U_{eq}, calculated as $U_{eq} = 1/3 \sum_i \sum_j U_{ij} a_i^* a_j^* A_{ij}$ where A_{ij} is the dot product of the i^{th} and j^{th} direct space unit cell vectors.

Appendix Table C-9: Bond Lengths (Å) and angles (°)for the non-H atoms of compound $(BEDT\text{-}TTF)PF_6$*

S(1)-C(1)	1.725(2)
S(1)-C(2)	1.743(2)
S(2)-C(1)	1.726(2)
S(2)-C(3)	1.741(2)
S(3)-C(2)	1.745(2)
S(3)-C(4)	1.818(2)
S(4)-C(3)	1.743(2)
S(4)-C(5)	1.808(2)
C(1)-C(1)#1	1.382(4)
C(2)-C(3)	1.357(3)
C(4)-C(5)	1.510(3)
P-F(3)	1.593(2)
P-F(3)#2	1.593(2)
P-F(2)	1.594(2)
P-F(2)#2	1.594(2)
P-F(1)#2	1.597(1)
P-F(1)	1.597(1)

C(1)-S(1)-C(2)	95.90(10)
C(1)-S(2)-C(3)	95.77(10)
C(2)-S(3)-C(4)	102.83(10)
C(3)-S(4)-C(5)	98.81(10)
C(1)#1-C(1)-S(1)	122.4(2)
C(1)#1-C(1)-S(2)	122.6(2)
S(1)-C(1)-S(2)	115.06(11)
C(3)-C(2)-S(1)	116.3(2)
C(3)-C(2)-S(3)	128.8(2)
S(1)-C(2)-S(3)	114.96(12)
C(2)-C(3)-S(2)	116.8(2)
C(2)-C(3)-S(4)	127.1(2)
S(2)-C(3)-S(4)	116.01(12)
C(5)-C(4)-S(3)	113.3(2)
C(4)-C(5)-S(4)	112.0(2)
F(3)-P-F(3)#2	180.0
F(3)-P-F(2)	90.42(11)
F(3)#2-P-F(2)	89.58(11)
F(3)-P-F(2)#2	89.58(11)
F(3)#2-P-F(2)#2	90.42(11)
F(2)-P-F(2)#2	180.0
F(3)-P-F(1)#2	90.10(9)
F(3)#2-P-F(1)#2	89.90(9)
F(2)-P-F(1)#2	88.94(9)
F(2)#2-P-F(1)#2	91.06(9)

F(3)-P-F(1)	89.90(9)
F(3)#2-P-F(1)	90.10(9)
F(2)-P-F(1)	91.06(9)
F(2)#2-P-F(1)	88.94(9)
F(1)#2-P-F(1)	180.0

#1 -x,-y+1,-z+2 #2 -x+1,-y+1,-z+1

Appendix Table C-9 : Anisotropic thermal parameters[a] (multiplied by 10^3) for the non-H atoms of compound (BEDT-TTF)PF_6*

	U11	U22	U33	U23	U13	U12
S(1)	22(1)	18(1)	25(1)	9(1)	5(1)	7(1)
S(2)	22(1)	20(1)	23(1)	10(1)	5(1)	5(1)
S(3)	19(1)	24(1)	30(1)	15(1)	8(1)	8(1)
S(4)	25(1)	27(1)	26(1)	12(1)	9(1)	13(1)
C(1)	21(1)	15(1)	20(1)	4(1)	0(1)	1(1)
C(2)	19(1)	14(1)	20(1)	7(1)	-1(1)	2(1)
C(3)	20(1)	15(1)	19(1)	5(1)	0(1)	3(1)
C(4)	20(1)	18(1)	26(1)	7(1)	2(1)	4(1)
C(5)	19(1)	22(1)	22(1)	9(1)	1(1)	5(1)
P	19(1)	14(1)	24(1)	4(1)	2(1)	3(1)
F(1)	49(1)	30(1)	45(1)	9(1)	17(1)	23(1)
F(2)	33(1)	31(1)	84(1)	25(1)	20(1)	1(1)
F(3)	70(1)	40(1)	39(1)	-2(1)	-23(1)	17(1)

[a] Uij are the mean-square amplitudes of vibration in $Å^2$ from the general temperature factor expressio

$\exp[-2\pi^2(h^2a^{*2}U11 + k^2b^{*2}U22 + l^2c^{*2}U33 + 2hka^*b^*U12 + 2hla^*c^*U13 + 2klb^*c^*U23)]$

Appendix Table C-10: Fractional coordinates and isotropic thermal parameters ($Å^2$) for the H atoms of compound (BEDT-TTF)PF_6*

Atom	x	y	z	U
H(4A)	-0.398(49)	1.2638(48)	0.7439(33)	0.035(8)
H(4B)	-0.574(44)	1.2038(40)	0.5867(30)	0.024(7)
H(5A)	-0.3528(44)	0.9520(43)	0.6154(29)	0.026(7)
H(5B)	-0.4054(45)	1.1482(42)	0.6584(28)	0.026(7)

LIST OF REFERENCES

1. Miller, J. S. *Extended Linear Chain Compounds;* Plenum Press: New York, 1983.

2. Cowan, D. O.; Wiygul, F. M. *Chem. Eng. News* **1986**, *July 21*, 28.

3. Adrian, F. J.; Cowan, D. O. *Chem. Eng. News* **1992**, *December 21*, 24.

4. Miller, J. S.; Epstein, A. J.; Reiff, W. M. *Chem. Rev.* **1988**, *88*, 201.

5. Haldane, F. D. M. *Phys. Lett.* **1983**, *93A*, 464.

6. Bonner J. C.; Fisher M. E. *Phys. Rev.* **1964**, *135*, A640.

7. Hatfield W. E.; Estes W. E.; Marsh W. E.; Pickens M. W.; Haar L. W.; Weller R. R. *J. Phys. Rev.* **1986**, *B33*, 702.

8. Bhatia S. N.; O'Connor C. J.; Carlin R. L.; Algra H. A.; de Jongh L. J. *Chem. Phys. Lett.* **1977**, *50*, 353.

9. Morosin B.; Graeber E. J. *Acta Cryst.* **1967**, *23*, 766.

10. Affeck, I. *J. Phys. Condens. Matter* **1989**, *1*, 3047.

11. Renard, J. P.; Gadet, V.; Regnault, L. P.; Verdaguer, M. *J. Magn. Magn. mater.* **1990**, *90*, 213.

12. Takeuchi, T; Hori, H.; Date, M.; Yosida, T.; Katsumata, K.; Renard, J. P.; Gadet, V.; Verdaguer, M. *J. Magn. Magn. Mater.* **1992**, *104*, 813.

13. Chou, L. -K.; Abboud, K. A.; Talham, D. R.; Kim W. W.; Meisel, M. W. *Chem. Mater.* **1994**, *6*, 2051.

14. Buyers, W. J. L.; Tun, Z.; Harrison, A.; Rayne, J. A.; Nicklow, R. M. *Physica B* **1992**, *180*, 222.

15. Nightingale, M. P.; Blote, H. W. J. *Phys. Rev.* **1986**, *B33*, 659.

16. Affleck, I. *Phys. Rev. B* **1992**, *46*, 9002.

17. Orendac, M.; Orendacova, J.; Cernak, J.; Feher, A.; Signore, P. J. C.; Meisel, M. W.; Merah, S.; Verdaguer, M. *Phys. Rev. B* **1995**, *52*, 3435.

18. Renard, J. P.; Verdaguer, M.; Regnault, L. P.; Erkelens, W. A. C.; Rossat-Mignod, J.; Stirling, W. G. *Europhys. Lett.* **1987**, *3*, 945.

19. Ajiro, Y,; Goto, T.; Kikuchi, H.; Sakakibara, T.; Inami, T.; *Phys. Rev. Lett.* **1989**, *63*, 1424.

20. Kini, A. M.; Geiser, U.; Wang, H. H.; Carlson, K. D.; Willams, J. M.; Kwok, W. K.; Vandervoort, K. G.; Thompson, J. E.; Stupka, D. L. *Inorg. Chem.* **1990**, *29*, 2555.

21. Kini, A. M.; Beno, M.A.; Carlson, K. D.; Ferraro, J. R.; Geiser, U.; Schultz, A. J.; Wang, H.H.; Williams, J. M.; Whangbo, M. -H. *The Physics and Chemistry of Organic Superconductors* **1990**, *51*, 334.

22. Crabtree, G. w.; Carlson, K. D.; Hall, L. N.; Copps, P. T.; Wang, H. H.; Emge, T. J.; Beno, M. A.; Williams, J. M. *Phys. Rev. B* **1984**, *30*, 2958.

23. Schegolev, I. F.; Yagubskii, E. B. Laukhin, V. N. *Mol. Cryst. Liq. Cryst.* **1985**, *126*, 365.

24. Emge, T. J.; Leung, P. C.; Beno, M. A.; Wang, H. H.; Firestone, M. A.; Webb, K. S.; Carlson, K. D.; Williams, J. M. *Mol. Cryst. Liq. Cryst.* **1986**, *132*, 363.

25. Williams, J. M.; Wang, H. H.; Emge, T. J.; Geiser, U.; Beno, M. A.; Carlson, K. D.; Thorn, R. J.; Schultz, A. J.; Whang, M. H. *Prog. Inorg. Chem.* **1987**, *35*, 51.

26. Wang, H. H.; Montgometry, L. K.; Husting, C. A.; Williams, J. M.; Budz, S. M.; Lowry, M. J.; Carlson, K. D.;Kwok, W. K.; Mikheyev, V. *Chem. Mater.* **1989**, *1*, 484.

27. Leung, P. C. W.; Emge, T. J.; Beno, M. A.; Wang, H. H.; Williams, J. M.; Petricek, V. Coppens, P. *J. Am. Chem. Soc.* **1985**, *107*, 6184.

28. Geiser, U.; Wang, H. H.; Budz, S. M.; Lowry, M. J.; Williams, J. M.; Ren, J.; Whangbo, M. H. *Inorg. Chem.* **1990**, *29*, 1611.

29. Geiser, U.; Wang, H. H.; Donega, K. M.; Anderson, B. A.; Williams, J. M.; Kwak, J. F. *Inorg. Chem.* **1986**, *25*, 401.

30. Geiser, U.; Wang, H. H.; Gerdom, L. E.; Firestone, M. A.; Sowa, L. M.; Williams, J. M.; Whangbo, M. H. *J. Am. Chem. Soc.* **1985**, *107*, 8305.

31. Williams, J. M.; Kini, A. M.; Wang, H. H.; Carlson, K. D.; Geiser, U.; Montgomery, L. K.; Pyrka, G. J.; Watkins, D. M.; Kwok, W. K. *Inorg. Chem.* **1990**, *29*, 3274.

32. Kinoshita, N.; Takahashi, K.; Murata, K.; Tokumoto, M.; Anzai, H. *Solid State Commun.* **1988**, *67*, 465.

33. Urayama, H.; Yamochi, H.; Saito, G.; Nozawa, K.; Sugano, T.; Kinoshita, M.; Sato, S.; Oshima, K.; Kawamoto, A.; Tanaka, J. *Chem. Lett.* **1988**, 55.

34. Pickett, W. E.; Krakauer, H.; Cohen, R. E.; Singh, D. J. *Science* **1992**, *255*, 46.

35. Beno, M. A.; Firestone, M. A.; Leung, P. C. W.; Wang, H. H.; Williams, J. M.; Whangbo, M. -H. *Solid State Commun.* **1986**, *57*, 735.

36. Chou, L. -K.; Abboud, K. A.; Talham, D. R.; Kim, W. W.; Meisel, M. W. *Physica B*, **1994**, *313-312*, 194.

37. Granroth, G. E.; Chou, L. -K.; Kim, W. W.; Chaparala, M.; Naughton, M. J.; Haanappel, E.; Lacerda, A.; Rickel, D.; Talham, D. R.; Meisel, M. W. *Physica B*, **1995**, *211*, 208.

38. Gadet, V.; Verdaguer, M.; Briois, V.; Gleizes, A.; Renard, J. P.; Beauvillain, P.; Chappert, C.; Goto, T.; Le Dang, K.; Veillet, P. *Phys. Rev. B* **1991**, *44*, 705.

39. Hitchman, M. A.; Rowbottom, G. L. *Coord. Chem. Rev.* **1982**, *42*, 55.

40. Goodgame, D. M. L.; Hitchman, M. A. *Inorg. Chem.* **1967**, *6*, 813.

41. Sheldrick, G. M. L.; SHELXTL plus; Nicolet XRD Corp.: Madison, WI, 1990.

42. *International Tables for X-ray Crystallography*; Kynoch Press: Birmingham, 1974: Vol. IV.

43. Cromer, D. T.; Mann, J. B. *Acta Crystallogr.* **1986**, *A24*, 321.

44. Cromer, D. T.; Liberman, D. *J. Phys. Chem.* **1970**, *53*, 1891.

45. Stewart, R. F.; Davidson, D. R.; Simpson. W. T. *J. Chem. Phys.* **1965**, *42*, 3175.

46. Finney, A. H. *Aust. J. Chem.* **1981**, *34*, 2125.

47. Stucky, G.; D'Agostino, S.; McPherson, G. *J. Am. Chem. Soc.* **1966**, *88*, 4828.

48. Asmussen, R. W.; Kindt Larsen, T.; Soling, H. *Acta Chem. Scand.* **1969**, *23*, 2055.

49. Avenel, O.; Xu, J.; Xia, J. S.; Xu, M.-F; Andraka, B.; Lang, T.; Moyland, P. L.; Ni, W.; Signore, P. J. C.; van Woerkens, C. M. C. M.; Adams, E. D.; Ihas, G. G.; Meisel, M. W.; Nagler, S. E.; Sullivan, N. S.; Takano, Y.; Talham, D. R.; Goto, T.; Fujiwara, N.; *Phys. Rev. B* **1992**, *46*, 8655.

50. Meyer, A.; Gleizes, A.; Girerd, J. J.; Verdaguer, M.; Kahn, O. *Inorg. Chem.* **1982**, *21*, 1729.

51. Weng, C. Y. Thesis, Carnegie Mellon University, 1968.

52. Renard, J. P.; Verdaguer, M.; Regnault, L. P.; Erkelens, W. A. C.; Rossat-Mignod; Ribas, J.; Stirling, W. G.; Vettier, C. *J. Appl. Phys.* **1988**, *63*, 3538.

53. Abragam, A.; Bleaney, B. *Electron Paramagnetic Resonance of Transition Metal Ions*: Clarendon Press: Oxford, **1970**, p911.

54. Koido, N.; Kambe, T.; Teraoka, S.; Hirai, S.; Goto, T.; Chou, L. -K.; Talham, D. R.; Meisel, M. W.; Nagata, K. *J. Magn, Magn, Mater.* **1995**, *140-144*, 1639.

55. Chou, L. -K.; Talham, D. R.; Kim, W. W.; Signore, P. J. C.; Meisel, M. W. *Physica B*, **1994**, *194-196*, 313.

56. Buyers, W. J. L.; Morra, R. M.; Armstrong, R. L.; Hogan, M. J.; Gerlach, P.; Hirakawa, K. *Phys. Rev. Lett.* **1986**, *56*, 371.

57. Affleck, I.; Kennedy, T.; Lieb, E. H.; Taski, H. *Phys. Rev. Lett.* **1987**, *59*, 799.

58. Glarum, S. H.; Geschwind, S; Lee, K. M.; Kaplan, M. L.; Michel, J. *Phys. Rev. Lett.* **1991**, *67*, 1614.

59. Gadet, V.; Verdaguer, M.; Renard, J. P.; Ribas, J.; Diaz, C.; Montfort, M.; Solans, X.; Landee, C. P.; Dworkin, A. *J. Am. Chem. Soc.* (submitted).

60. Zheludev, A.; Shapiro, S. M.; Nagler, S. E.; Chou, L.-K.; Talham, D. R.; Meisel, M. W. *Phys. Rev. B* (to be published)

61. Chou, L. -K.; Quijada, M. A.; Clevenger, M. B.; de Oliveira, G. F.; Abboud, K. A.; Tanner, D. B.; Talham, D. R. *Chem. Mater.* **1995**, *7*, 530.

62. Chou, L. -K.; Clevenger, M. B.; de Oliveira, G. F.; Abboud, K. A ; Talham, D. R. *Synth. Met.* **1995**, *70*, 1125.

63. Ferraro, J. M.; Williams, J. M. *Introduction to Synthetic Electrical Conductors*; Academic: San Diego, 1987.

64. Williams, J. M.; Ferraro, J. R.; Thorn, R. J.; Carlson, K. D.;Geiser, U.; Wang, H. H.; Kini, A. M.; Whangbo, M. H. *Organic Superconductors*; Simon & Schuster: Englewood Cliffs, NJ. 1992

65. Larsen, J.; Lenoir, C. *Synthesis* **1988**, *2*, 134.

66. Lee, M. M.; Stokes, J. P.; Wiygul, F. M.; Kistenmacher, T. J.; Cowan, D. O.; Poehler, T. J.; Bloch, A. N.; Fuller, W. W.; Gubser, D. U. *Mol. Cryst. Liq. Cryst.* **1982**, *79*, 501.

67. Torrance, J. B.; Scott, B. A.; Welber, B.; Kaufman, F. B.; Seiden, P. E. *Phys. Rev. B* **1979**, *19*, 730.

68. Sugano, T.; Yakushi, K.; Kuroda, H. *Bull. Chem. Soc. Jpn.* **1978**, *51*, 1041.

69. Kobayashi, H.; Kobayashi, A.; Sasaki, Y.; Saito, G. *Bull. Chem. Soc. Jpn.* **1986**, *59*, 301.

70. Kobayashi, H.; Kobayashi, A.; Sasaki, Y.; Saito, G.; Enoki, T.; Inokuchi, H. *J. Am. Chem. Soc.* **1983**, *105*, 297.

71. Abboud. K. A.; Clevenger. M. B.; de Oliveira G. F.; Talham, D. R. *J. Chem. Soc., Chem, Commun.*, **1993**, *20*, 1560.

72. Korotkov, V. E.; Shibaeva, R. P. *Sov. Phys. Crystallogr.* **1989**, *34*, 865.

73. Mori, T.; Wang, P.; Inokuchi, H. *Bull. Chem. Soc. Jpn.* **1988**, *61*, 591.

74. Mori, T.; Wang, P.; Imaeda, T.; Inokuchi, H. *Solid State Commun.* **1987**, *64*, 733.

75. Beno, M. A.; Geiser, U.; Kostka, K. L; Wang, H. H.; Webb, K. S.; Firestone, M. A.; Carlson, K. D.;Nunez, L.; Whangbo, M.; Williams, J. M. *Inorg. Chem.* **1987**, 1912.

76. Mori, T.; Kobayashi, A.; Sasaki, Y.; Kobayashi, H.; Saito, G.; Inokuchi, H. *Chem. Lett.* **1982**, 1963.

77. Day, P.; Kurmoo, M.; Mallah, T.; Marsden, I. R.; Friend, R. H.; Pratt, F. L.; Hayes, W.; Chasseau, D.; Gaultier, J.; Bravic, G.; Ducasse, L. *J. Am. Chem. Soc.* **1992**, *114*, 10722.

78. Umland, T. C.; Allie, S.; Kuhlmann, T.; Coppens, P. *J. Phys. Chem.* **1988**, *92*, 6456.

79. Quijada, M. A. Thesis, University of Florida, 1994.

80. Drozdova, O. O.; Semkin, V. N.; Vlasova, R. M.; Kushch, N. D.; Yagubskii, E. B. *Synth. Met.* **1994**, *64*, 17.

81. Abboud, K. A.; Chou, L. -K.; Clevenger, M. B.; Oliveira, G. F.; Talham, D. R. *Acta Cryst.* **1995**, C51, 2356.

82. Kurmoo, M.; Talham, D. R.; Day, P.; Parker, I. D.; Friend, R. H.; Stringer, A. M.; Howard, J. A. K. *Solid State Commun.* **1986**, *61*, 459.

83. Wang, H. H.; Carlson, K. D.; Geiser, U.; Kwok, W. K.; Vashon, M. D.; Thompson, J. E.; Larson, N. F.; McCabe, G. D.; Hulscher, R. S.; Williams, J. M. *Physica C* **1990**, *166*, 57.

84. Venturini, E. L.; Azevedo, L. J.; Schirber, J. E.; Williams, J. M.; Wang, H. H. *Phys. Rev. B: Condens. Matter* **1985**, *32*, 2819.

85. Kurmoo, M.; Green, M. A.; Day, P.; Bellitto, C.; Staulo, G.; Pratt, F. L.; Hayes, W. *Synth. Met.* **1993**, *55*, 2380.

86. Geiser, U.; Wang, H. H.; Williams, J. M.; Venturini, E. L.; Kwak, J. F.; Whangbo, M. H. *Synth. Met.* **1987**, *19*, 599.

87. Porter, L. C.; Wang, H. H.; Beno, M. A.; Carlson, K. D.; Pipan, C. M.; Proksch, R. B.; Williams, J. M. *Solid State Commun.* **1987**, *64*, 387.

88. Bu, X.; Cisarova, I.; Coppens, P. *Acta Cryst.* **1992**, *C48*, 1564.

89. Bray, J. W.; Interrante, L. V.; Jacobs, I. S.; Bonner, J. C. *In Extended Linear Chain Compound* ; Miller, J. S., Ed., Plenum Press: New York, 1983, p353.

90. Bloch, D; Voiron, J.; de Jongh, L. J. *High field magnetism* ; Elsevier: North Holland, 1983.

91. Bu, X.; Cisarova, I.; Coppens, P. *Acta Cryst.* **1992**, *C48*, 1562.

92. Mabbs, F. E.; Machin, D. J. *Magnetism and Transition Metal Complexes*, Chapmon and Hall: London, 1973.

93. Shibaeva, R. P.; Lobkovskaya, R. M.; Kaminskii, V. F.; Lindeman, S. V.; Yagubskii, E. B. *Kristallografiya* **1986**, *31*, 920; *Sov. Phys. Crystallogr.* (Engl. Transl.) **1986**, *31*, 546.

94. Wooten, F. *Optical Properties of Solids*; Academic: New York, 1972.

95. Rice, M. J.; Yartsev, V. M.; Jacobsen, C. S. *Phys. Rev. B*, **1980**, *21*, 3437.

96. Bu, X.; Cisarova, I.; Coppens, P. *Acta Cryst.* **1992**, *C48*, 1558.

BIOGRAPHICAL SKETCH

Liang-Kuei Chou was born in Chung-Li, Taiwan on September 24, 1964 to Chao-Feng and Chun-Chih Chou. After graduating from the High School of National Taiwan Normal University (Taipei) in 1983, he attended Soochow University (Taipei) and majored in chemistry until 1987 when he obtained a Bachelor of Science in chemistry. From 1987 to 1989, Chou served in the army; he is second-lieutenant instructor in National Defense Department (Taiwan). After completing his service, he attended the National Taiwan University and earned a Master of Science degree in 1991 under Dr. Yu Wang. He then come to Gainesville, Florida, to pursue graduate studies in chemistry in 1991 under Dr. Daniel R. Talham. Upon completion of his doctorate, Chou plans to do postdoctoral work.

I certify that I have read this study and that in my opinion it conforms to acceptable standards of scholarly presentation and is fully adequate, in scope and quality, as a dissertation for the degree of Doctor of Philosophy.

Daniel R. Talham, Chairman
Associate Professor of Chemistry

I certify that I have read this study and that in my opinion it conforms to acceptable standards of scholarly presentation and is fully adequate, in scope and quality, as a dissertation for the degree of Doctor of Philosophy.

Russell S. Drago
Graduate Research Professor of Chemistry

I certify that I have read this study and that in my opinion it conforms to acceptable standards of scholarly presentation and is fully adequate, in scope and quality, as a dissertation for the degree of Doctor of Philosophy.

William R. Dolbier
Professor of Chemistry

I certify that I have read this study and that in my opinion it conforms to acceptable standards of scholarly presentation and is fully adequate, in scope and quality, as a dissertation for the degree of Doctor of Philosophy.

James M. Boncella
Associate Professor of Chemistry

I certify that I have read this study and that in my opinion it conforms to acceptable standards of scholarly presentation and is fully adequate, in scope and quality, as a dissertation for the degree of Doctor of Philosophy.

Mark W. Meisel
Associate Professor of Physics

This dissertation was submitted to the Graduate Faculty of the Department of Chemistry of the College of Liberal Arts and Sciences and to the Graduate School and was accepted as partial fulfillment of the requirements for the degree of Doctor of Philosophy.

May, 1996

Dean, Graduate School